4-12-2021

Hybrid Lattice Boltzmann Agglomeration Method for Modeling Transport Phenomena in Polymer Electrolyte Membrane Fuel Cells

P. Satjaritanun

F. C. Cetinbas

S. Hirano

I. V. Zenyuk

R. K. Ahluwalia

See next page for additional authors

Publication Info

Published in *Journal of The Electrochemical Society*, Volume 168, 2021, pages 044508-.

Author(s)

P. Satjaritanun, F. C. Cetinbas, S. Hirano, I. V. Zenyuk, R. K. Ahluwalia, and Sirivatch Shimpalee

Journal of The Electrochemical
Society

Hybrid Lattice Boltzmann Agglomeration Method for Modeling Transport Phenomena in Polymer Electrolyte Membrane Fuel Cells

To cite this article: P. Satjaritanun *et al* 2021 *J. Electrochem. Soc.* **168** 044508

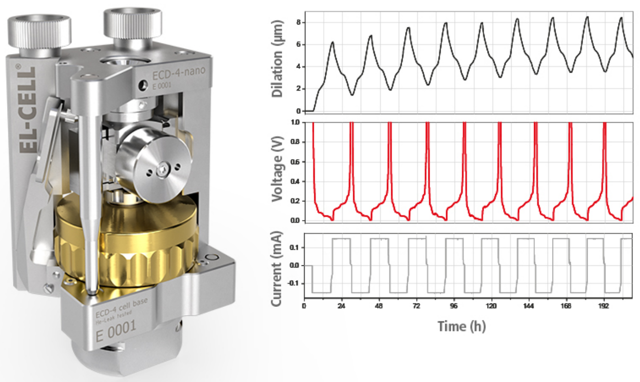

Journal of The Electrochemical Society, 2021 **168** 044508

Hybrid Lattice Boltzmann Agglomeration Method for Modeling Transport Phenomena in Polymer Electrolyte Membrane Fuel Cells

P. Satjaritanun,[1,2,*] F. C. Cetinbas,[3] S. Hirano,[4] I. V. Zenyuk,[2,*] R. K. Ahluwalia,[3] and S. Shimpalee[1,*,z]

[1] *Department of Chemical Engineering, The University of South Carolina, Columbia, South Carolina, United States of America*
[2] *Department of Chemical Engineering and Material Science; National Fuel Cell Research Center, University of California, Irvine, California, United States of America*
[3] *Argonne National Laboratory, Energy Systems Division, Illinois, United States of America*
[4] *Ford Motor Company, Research, and Innovation Center, Dearborn, Michigan, United States of America*

The Hybrid Lattice Boltzmann Agglomeration Method (HLBAM) was employed to model transport phenomena and electrochemical kinetics in the catalyst layer of a polymer electrolyte membrane fuel cell (PEMFC). This work showed the advantages of using a direct modeling-based HLBAM approach, which incorporates the detailed structure of catalyst layers from X-ray computed tomography as well as local transport variables related characteristics and effective properties from the hybrid catalyst microstructure. The local transport variables and effective properties from the hybrid catalyst model were used to simulate the electrochemical kinetics inside the detailed structure of the catalyst layer. HLBAM can predict the distribution of local effective transport variables and electrochemical kinetics during cell operation. The studies included the prediction of liquid water saturation/evolution, heat transfer, species transport, and electrochemical kinetics inside the porous and catalyst layers relevant to fuel cell operation. HLBAM enables one to distinguish electrochemical distribution in the triple-phase boundaries at the catalyst sites. This method can expedite the development of porous components in PEMFCs in a cost-effective manner. The HLBAM simulation can assist the optimization of porous medium design and durability as well as provide insights into water management, particularly in the catalyst layer.

[DOI: 10.1149/1945-7111/abf217]

Manuscript submitted December 2, 2020; revised manuscript received March 12, 2021. Published April 12, 2021. *This was paper 2100 presented during PRiME 2020, October 4–9, 2020.*

List of Symbols

a_{agg}	effective agglomerate surface area
a_{Pt}	active surface area of platinum
a_{Pt}^{eff}	effective reaction surface area
$C_{H_2}^{ref}$	reference hydrogen concentration
$C_{O_2}^{ref}$	reference oxygen concentration
D_{eff}	effective diffusivity of dissolved reactant in Nafion™
$D_{\varnothing}^{eff}$	effective diffusion coefficient of proton conductivity
D_{H_2}	diffusivity of the dissolved hydrogen in Nafion™
D_{O_2}	diffusivity of the dissolved oxygen in Nafion™
E_{act}	activation energy
E_r	effectiveness factor of the spherical agglomerate
F	Faraday's constant
H	Henry's constant
i	current per unit volume in the CL
i_{agg}	agglomerate volumetric current density
$i_{o,a}$	anode exchange current density
$i_{o,c}$	cathode exchange current density
$i_{o,a}^{ref}$	reference anode exchange density
$i_{o,c}^{ref}$	reference cathode exchange density
k_a	reaction rate at the surface of the agglomerate core of anode
k_c	reaction rate at the surface of the agglomerate core of cathode
m_{Pt}	platinum loading
n	number of electrons
P_{H_2}	hydrogen pressure
P_{O_2}	oxygen pressure
$P_{H_2}^{ref}$	reference hydrogen pressure
$P_{O_2}^{ref}$	reference oxygen pressure
R	ideal gas constant
r_{agg}	agglomerate radius
T	local temperature
T_0	refence temperature
t_{CL}	catalyst layer thickness
V	total volume that agglomerate and thin film occupy
V_{agg}	agglomerate volume

Greek symbols

α_a	anode charge transfer coefficient
α_c	cathode charge transfer coefficient
δ	thickness of the Nafion™ film
ε_{CL}	catalyst layer porosity
η_a	anode overpotential
η_c	cathode overpotential
$\varnothing_L$	Thiele's modulus
$\varnothing_m$	electrolyte potential
ρ_{Pt}	platinum density

In the development and commercialization of electrochemical energy technologies for renewable energy have existed over past centuries, fuel cells became the electric power sources of future generation automobiles[1–6] and heavy-duty transportation.[7] Fuel cells are designed to operate on zero-carbon hydrogen as a fuel, which is a good way to reduce emissions for small stationery and transportation applications. Polymer electrolyte membrane fuel cell (PEMFC) is one type of fuel cell that operates at a significantly low temperature, which is a strong candidate for vehicles and the generation of electricity.

Over the past decades, significant progress has been made in enhancing PEMFC performance and durability. Understanding how

---

*Electrochemical Society Member.

[z]E-mail: shimpale@cec.sc.edu

the PEMFC performs, including mass transports and electrochemical kinetics of each particular design and cell operating condition, will lead the developers toward improved cell designs as well as increased performance and durability. Multi-scale fuel cell models[8,9] have been developed to understand the transport phenomena and electrochemical kinetic in the catalyst layer and porous media of PEMFCs. The modeling of related transport phenomena on the catalyst layer is still challenging and required attention.[10] Computational Fluid Dynamics (CFD) is a mathematical modeling tool used to perform numerical analysis to analyze and solve the local transport problems in the PEMFCs. Experimental investigations of locally transport phenomena inside catalyst and porous media in the operating cell are incomprehensible. CFD incorporates theory and experimentation in the field of electrochemical kinetics, heat, and mass transport for PEMFC, which allowed us to explore understanding into activities and transport phenomena that cannot be observed through experiments.

Three-dimensional (3D) direct modeling-based Lattice Boltzmann method (LBM)[9,11,12] is one of the CFD techniques that can be used to solve the water management problem and analyze the local transport phenomena inside the detailed structure of the porous and catalyst layers of PEMFCs. The porous structures of the PEMFC consist of gas diffusion layer (GDL), microporous layer (MPL), and catalyst layer (CL). These detailed structures of porous medium were obtained from the micro and nano X-ray computed tomography (CT), which is at the micro-scale level. Conventional CFD (i.e., Navier–Stokes equations based)[6,13–26] appears to be inappropriate for modeling transport inside the detailed structure of porous medium due to its complexity of mesh generation method.[8] Pore-network modeling (PNM)[27–33] is also one of the simulation techniques used to model the transport inside the porous structure of PEMFCs. The model geometry in PNM is a stochastic pore structure, which is interconnections of cylindrical pores. PNM generated the pore structure by using measurement information such as pore size distribution, capillary pressure, and saturation relationship.[10] However, PNM used a lot of computational resources and time to complete the numerical simulation.[10] LBM is a novel particle-based simulation that has been designed to perform the calculation based on the non-equilibrium statistical mechanics and gas modeled at a microscopic scale, which is proper to model the transport phenomena inside the micro-scale porous medium. The lattice particle meshing approach in the LBM avoids the classic domain meshing process and the surface complexity. Hence, the LBM simulation becomes widely used when modeling transport inside the complex structures in PEMFCs.

Several researchers used the LBM simulation to model the transport phenomena inside the porous medium of PEMFCs,[11,12,34–41] where few studies have clarified the mechanism of electrochemical kinetics, species transport as well as the transport behavior of liquid water through the porous layer and CL. Sepe et al.,[34] used the LBM with the detailed geometries from X-ray CT to understand the mass transport properties through the GDL samples. They found that the liquid saturation inside the sample is dependent on the structure of the GDL. The change of morphology properties such as pore structure, permeability, and orientation in both in-plane and through-plane control the transport pathways that liquid water must take, which would help or impact PEMFC performance. The wettability has also impacted the dynamics of liquid water while removing it from the GDL. Shakerinejad et al.[35] performed the LBM simulation to study the effects of mixed-wettability on liquid water transport in the stochastic pore structure of GDL. They showed the correlation of surface wettability and the merging process of water clusters, which concluded that hydrophobic conditions led to a decrease in the effective water cluster and merging process in the GDL. The study also suggests that a hydrophilic environment near the GDL and channel interface can accelerate the water removal and enhance cell performance. Garcia-Salaberri et al.[38,39] used the LBM combine with the 3D geometry of GDL from micro X-ray CT to study the transport inside the porous medium. They concluded that the LBM could manage complex geometry simulation and possible to model the liquid water saturation, effective diffusivity, permeability, and effective electrical/thermal conductivity inside the GDL samples. These studies also showed that the detailed structure of the porous medium plays a major role in water transport inside the PEMFC. However, these researchers did not include the effect of cell operating conditions that impacted the transport phenomena, such as cell temperature, evaporation/condensation rate, as well as the current density.

A few researchers used LBM to model the electrochemical kinetics and mass transport inside the detailed structure of CL. Zhang et al.[42] simulated the liquid water transport and oxygen diffusion in the cathode of a PEMFC with an electrochemical reaction model. However, their GDL and CL geometries were not replicas of real samples. In the previous work,[9] the LBM was incorporated with the detailed structure of the CL to predict the electrochemical kinetics distribution inside the CL of PEMFC. The detailed geometry of the CL was obtained from nano X-ray CT, which provides the inside agglomerate structure detail of CL such as ionomer thin-film, platinum (Pt), and carbon support (Cs). This previous work also showed the success in integrating the lattice elements into an agglomerate structure to perform the kinetic prediction by LBM simulation, which this model is known as Lattice Boltzmann Agglomeration Method (LBAM).[9] However, the LBAM model still lacks information on local transport properties such as effective diffusivity of oxygen and ionomer thin-film thickness. Cetinbas et al.,[43–45] demonstrated a hybrid approach to characterize the detailed structure of the CL from micro to nano scale by combining different experimental techniques. This approach provides a complete description of 3-D electrode microstructure by including details of carbon support, catalyst, ionomer, and primary pores directly within the 3-D X-ray CT images which are limited to resolve the electrode morphology as secondary pores and solid structure. Structure generated via this method is a hybrid combination of X-ray data and experimental data based stochastic reconstruction technique and is referred as hybrid catalyst microstructure (HCM)[43] in this study.

In this work, the HCM has been introduced into the LBAM model[9] to improve the modeling fidelity prediction of local transport properties computation and electrochemical variables of PEMFC. This newly developed method developed in this work is called the Hybrid Lattice Boltzmann Agglomeration Method (HLBAM). Figure 1 shows the conceptual multiscale modeling HLBAM approach. The Boltzmann transport equation is used to solve the heat and mass transport inside the GDL/MPL and CL. This model geometry (i.e., GDL/MPL and CL) provided in this study will be obtained by 3D reconstructed microstructure from multiscale image techniques such as micro and nano X-ray CT. The GDL sample used in this work is the SGL 25BC. This GDL has a porosity of 0.78 with the average contact angle of 110.[46] The membrane is similar to Nafion^{TM} 211. The CT images of GDL/MPL and CL had a voxel resolution of 1.33 and 0.01 μm, respectively. The detailed structure of the catalyst sample and HCM structure was created by Ion Power and was used by Cetinbas et al.[43] The structure of the HCM element is modeled to distinguish three-phase boundaries, carbon support (electron transfer), ionomer (proton transfer), and platinum particles (reaction). The bridging method is used to transfer the transport properties between the HCM and CL, which allows transport data to be transferred from local effective catalyst sites to the CL. Catalyst layer modeling utilizing the HLBAM is used to predict local transport properties, as well as solve the chemical reaction of oxygen (O_2) and hydrogen (H_2) in both catalyst geometries at the same time. The commercial software XFlow 2020 Refresh 1 Beta (Build 108.07) incorporate with MATLAB® is used to perform the CFD simulation. Through this modeling method, the local transport properties and characteristics of the electrochemical kinetics expression, such as liquid water saturation, O_2, water vapor, overpotential, electron transfer, and exchange current will be investigated under different cell operating conditions.

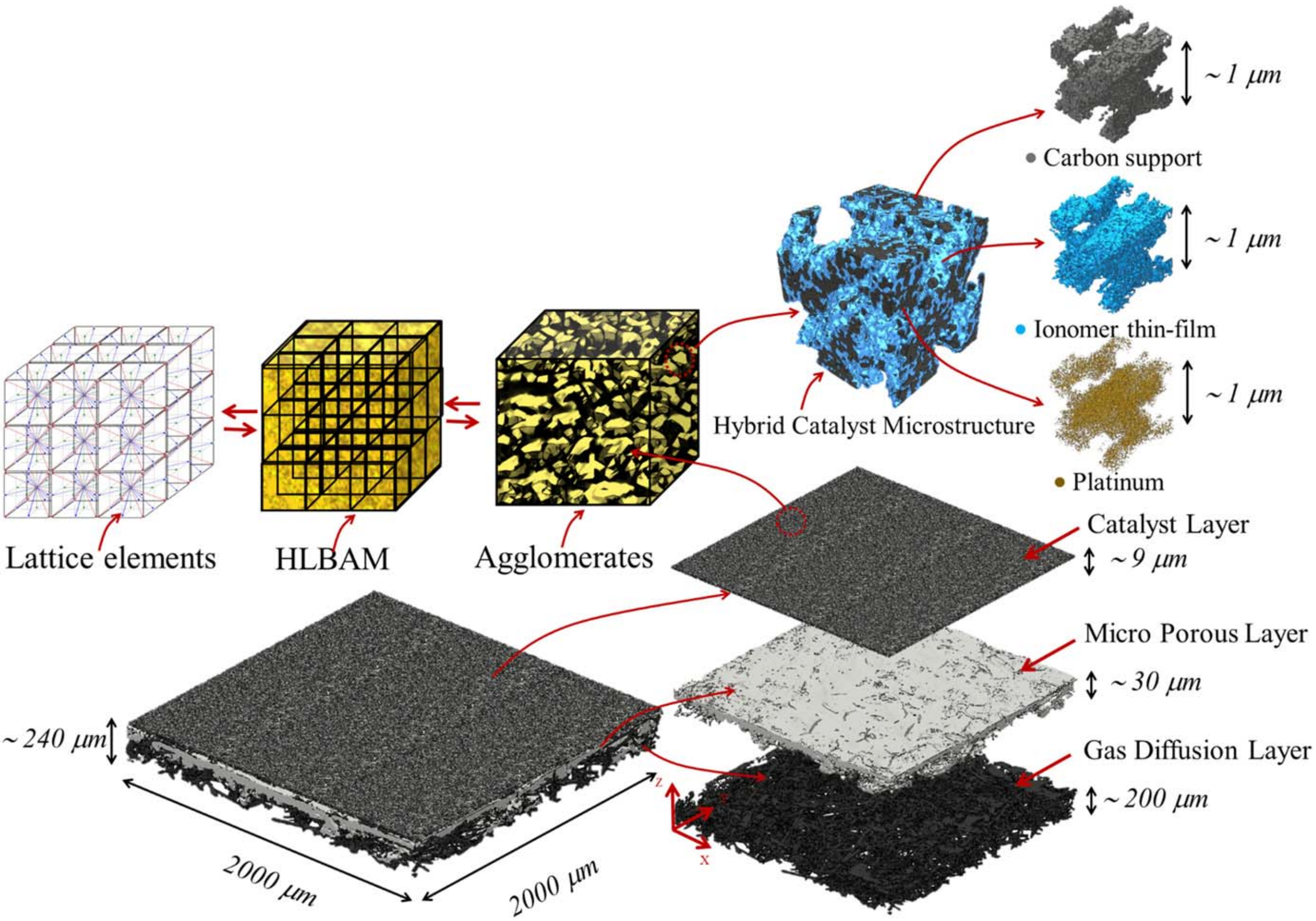

Figure 1. Conceptual of HLBAM approach and the detailed structure of the GDL/MPL sample (SGL25BC), CL sample (Ion Power) from both micro and nano X-ray CT, and hybrid catalyst microstructure.

Model development.—Hybrid Lattice Boltzmann Agglomeration Method (HLBAM) is the direct modeling-based, which is used to perform the numerical solution of electrochemical kinetics and multi-scalar/physic transport within the detailed structure of CL. This method has been improved by introducing the HCM into the Lattice Boltzmann Agglomeration Method (LBAM),[9] which can investigate the local effective transport variables (i.e., diffusivity, proton, and scalar). The co-simulation approach[8] was implemented to combine three main simulation techniques (i.e., macroscale model,[6,13] microscale LBM,[11,12] and HLBAM) and perform numerical calculation simultaneously. Figure 2a presents the conceptual of co-simulation approach with the method of shared interfacial boundary and data mappers technique. The macroscale model, Navier–Stokes (N-S) equation-based, simulated the transport in the bipolar plate, flow-field, and membrane. Then, the data mapping approach[8] transferred the local transport properties at the shared interface boundary into the microscale LBM (GDL/Flow-field interface) and HLBAM (CL/Membrane interface). The microscale LBM solved the transport in the GDL/MPL and transferred the transport properties into the HLBAM (MPL/CL interface) at shared boundary interfaces. The HLBAM generated in this work was used to predict the distribution of electrochemical variables and multi-physics/scalar in both detailed structure and HCM at the same time. After All, the co-simulation approach performed a parallel calculation within the multiscale domain, which allows the connection between each simulation technique and enables to transfer of the transport properties back and forth.

Figure 2b shows the bridging method of HLBAM which provides the detailed conceptual bridge between modeling of detailed structure CL and HCM. The Bridging method was applied to transfer data between HCM and agglomerate CL. At the detailed structure CL, the lattice matrix (2000 × 2000 × 1 μm^3) was created in the x–y plane which represents the local position of the catalyst site, which consists of 6,400 catalyst sites. Then, the bridging method was used to transfer the transport properties from local catalyst sites of detailed CL structures to the HCM (1 × 1 × 1 μm^3) for performing the HLBAM simulation. This Bridging method enables data transfer between many catalyst elements within reasonable computational time. After that, the co-simulation approach was used to perform parallel simulation in both computational domains, which allowed both models to bridge the transport properties exchange. The simulation was computed until the results reach steady-state or expected times. The convergence criteria for LBM simulation uses the evaluation of stability parameter (S). This parameter was calculated each of time step and it gives an awareness of the stability and the steady state point of the simulation. The recommend stability parameter for the multiphase flow model should have a value between 0.05 to 1.

$$S = \frac{\max\left(S_{\vartheta},\ S_{v},\ S_{\rho}\right)}{0.7} \qquad [1]$$

where S_{ϑ} is the numerical kinematic viscosity, S_v is the numerical kinematic velocity, and S_ρ is the numerical kinematic density. Below is an explanation of the specific model applied to this work.

Lattice Boltzmann method.—In this work, the Boltzmann transport equation was used to solve the transport in the GDL and MPL computational domain. LBM was developed as an improved modification of the Lattice Gas Cellular Automata (LGCA) to improve the

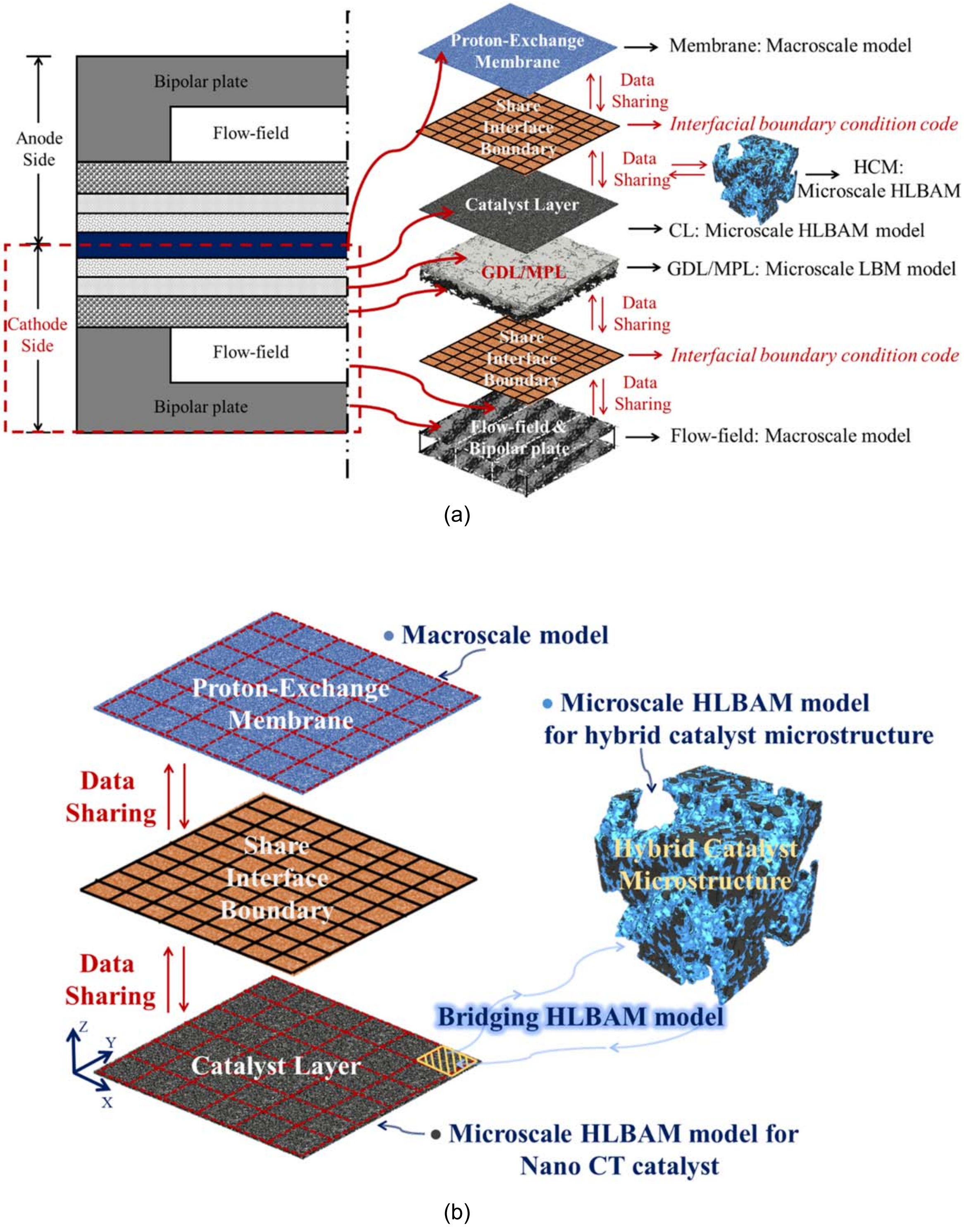

Figure 2. (a) Co-simulation approach with the method of interfacial boundary condition transfer and data mappers: Macroscale model, Microscale LBM, and HLBAM. (b) The bridging model of HLBAM provides a conceptual bridge of local transport properties between catalyst sites on the detailed structure of the catalyst layer and the hybrid catalyst microstructure.

inertial frame of reference (Galilean invariance) and eliminate statistical noise. Since LBM is a particle-based model. Therefore, the meshing process is removed and replaced by the Octree structure lattice elements. LBM is an appropriate CFD technique for solving complicated fluid flow problems in complex geometries such as a detailed structure of GDL/MPL and CL. The streaming and collisions scheme of the lattice particles can be interpreted as a discrete approximation of the continuous Boltzmann equation. In the continuum space with discrete velocities, Boltzmann's transport equation is defined as follows:

$$f_j(\vec{x} + \vec{e}_j\Delta t,\, t + \Delta t) - f_j(\vec{x},\, t) = \Omega_j(f_1(\vec{x},\, t),\ldots,(f_b(\vec{x},\, t)),\quad j = 1,\ldots,b \qquad [2]$$

where f_j is the particle distribution function in direction j, $\vec{e}_j$ is the particle discrete velocity, and Ω_j is the collision operator. The detailed LBM in the PEMFC model has already been provided in the previous works.[8,9,11,12]

Hybrid lattice Boltzmann agglomeration method.—The HLBAM has been established to perform numerical analysis of electrochemical kinetics and transport phenomena in both the detailed structure of the CL and HCM. This method has been enhanced from the previous LBAM model[9] by introducing an HCM[43] into the computational domain, which incorporates the local transport variables related characteristics and effective properties. As mentioned above, in the whole CL computational domain, HLBAM was used to predict the local transport and effective properties in the HCM. These properties were transferred into the detailed structure of CL by using the bridging method and co-simulation approach. Then, HLBAM predicted the distribution of electrochemical variables and other transport phenomena inside the CL computational domain.

The HLBAM kinetic expression has been improved from the basic Butler-Volmer equation and agglomerate model,[14,24,26,47–54] which considers H_2 and O_2 transport and diffusion within the ionomer thin film of the agglomerate. The kinetic variables in the CLs were provided by numerical solution of the agglomerate model. The electrochemical kinetics expression of HLBAM is presented as the following equations:

$$i_{agg} = \frac{nF\bar{V}_{agg}P_{O_2}}{H_{O_2}}\left[\left(\frac{r_{agg}^2\delta_{agg}}{3D_{O_2}(r_{agg}+\delta_{agg})} + \frac{1}{E_r k_c(1-\varepsilon_{CL})}\right)^{-1}\right] \tag{3}$$

$$i_{agg} = \int_{V_{agg}} i dV = \int_0^{r_{agg}} 4\pi r^2 \cdot i dr \tag{4}$$

$$\bar{V}_{agg} = \frac{r_{agg}^3}{(r_{agg}+\delta_{agg})^3} \tag{5}$$

where i_{agg} is the total agglomerate volumetric current density, i is the current per unit volume in the CL, n is the number of electrons involved in the reaction per mole of reactant, F is the Faraday's constant, P_{O_2} is the O_2 pressure, H_{O_2} is Henry's constant of O_2, E_r is an effectiveness factor of the spherical agglomerate, k_c is the reaction rate at the surface of the agglomerate core, ε_{CL} is the CL porosity, $\bar{V}_{agg}$ is the active area scaling factor, r_{agg} and r is the local agglomerate radius, $\bar{V}_{agg}$ is the average agglomerate volume, V_{agg} is the total volume that agglomerate and thin-film occupy, δ_{agg} is the local thickness of the Nafion^{TM} thin film, and D_{O_2} is local the diffusivity of the dissolved O_2 in the Nafion^{TM} membrane. In this work, the local agglomerate radius is provided by the detailed structure properties in the CL and can be calculated by the following equation:

$$r_{agg} = \left[\frac{4}{3}\pi(1-\varepsilon_{CL})(2r_{lattice})^3\right]^{\frac{1}{3}} \tag{6}$$

where $r_{lattice}$ is the local lattice radius that represents the pore radius inside the agglomerate of catalyst. The local diffusivity of O_2 (D_{O_2}) is provided by the relationship of molecular diffusion and Knudsen diffusion as shown in the following equation:

$$\frac{1}{D_{O_2}} = \frac{1}{D_{O_2,bulk}} + \frac{1}{\frac{2r_{agg}}{3}\sqrt{\frac{8RT}{\pi M_{O_2}}}} \tag{7}$$

where $D_{O_2,bulk}$ is the bulk diffusion of O_2 and M_{O_2} is the molecular mass of O_2. The effective diffusion coefficient of reactance gases describes diffusion through the pore space of porous material. The effective diffusion coefficient of O_2 transport through the pores ($D_{O_2,eff}$) can be presented as the following equation:

$$D_{O_2,eff} = \frac{D_{O_2}\varepsilon_{CL}\delta_c}{\tau} \tag{8}$$

where τ is the tortuosity, and δ_c is the dimensionless constrictivity. The reaction rate at the surface of the agglomerate core of the cathode side is shown below:

$$k_c = -\frac{a_{Pt}^{eff} i_{o,c}}{nFC_{O_2}^{ref}}\left[\exp\left(\frac{-\alpha_c F}{RT}\eta_c\right) + \exp\left(\frac{(1-\alpha_c)F}{RT}\eta_c\right)\right] \tag{9}$$

where a_{Pt}^{eff} is the effective reaction surface area, $i_{o,a}$ is the anode exchange current density, $i_{o,c}$ is the cathode exchange current density, R is the ideal gas constant, T is the local temperature, $C_{O_2}^{ref}$ is the reference O_2 concentration, and α_c is the cathode charge transfer coefficient. The kinetic expression used in the HLBAM to calculate the over-potential for both the cathode and anode CLs that involve activation and concentration overpotential are shown below:

$$\eta_a = \frac{RT}{\alpha_a F}\ln\left[\frac{i \times P_{H_2}^{ref}}{i_{0,a} \times P_{H_2}}\right] + \frac{RT}{2F}\ln\left[\frac{P_{H_2}^{ref}}{P_{H_2}}\right] \tag{10}$$

$$\eta_c = \frac{RT}{\alpha_c F}\ln\left[\frac{i \times P_{O_2}^{ref}}{i_{0,c} \times P_{O_2}}\right] + \frac{RT}{4F}\ln\left[\frac{P_{O_2}^{ref}}{P_{O_2}}\right] \tag{11}$$

where η_a is the local anode overpotential, η_c is the local cathode overpotential, α_a is the anode charge transfer coefficient, $P_{H_2}^{ref}$ is the reference H_2 pressure or H_2 inlet pressure, $P_{O_2}^{ref}$ is the reference O_2 pressure or O_2 inlet pressure. The effective reaction area (a_{Pt}^{eff}) is a function of specific platinum surface area per unit CL volume (a_{Pt}), Pt loading (m_{Pt}), Pt density (ρ_{Pt}), CL thickness (t_{CL}), and the CL porosity (ε_{CL}), are used to calculate the effective reaction area for the portions of the CL that are unable to encounter the requirements for the electrochemical reaction:

$$a_{Pt}^{eff} = \frac{a_{Pt}m_{Pt}}{\rho_{Pt}t_{CL}(1-\varepsilon_{CL})} \tag{12}$$

The anode ($i_{o,a}$) and the cathode ($i_{o,c}$) exchange current densities are a function of the reference exchange density, activation energy (E_{act}), and local temperature. The anode exchange current density and cathode exchange density are shown in the equations below:

$$i_{o,a} = i_{o,a}^{ref}\exp\left[\frac{-\Delta E_{act}}{R}\left(\frac{1}{T} - \frac{1}{T_0}\right)\right] \tag{13}$$

$$i_{o,c} = i_{o,c}^{ref}\exp\left[\frac{-\Delta E_{act}}{R}\left(\frac{1}{T} - \frac{1}{T_0}\right)\right] \tag{14}$$

The effectiveness factor (E_r) of the spherical agglomerate is obtained by the analytical solution of the effectiveness of the electrode reaction. This can be explained as a ratio of the actual reaction rate to the rate if the entire interior surface is exposed to the conditions outside of the particle.[26] The effectiveness factor is shown in the following equation:

$$E_r = \frac{1}{\varnothing_{L,c}}\left(\frac{1}{\tanh(3\varnothing_{L,c})} - \frac{1}{3\varnothing_{L,c}}\right) \tag{15}$$

where $\varnothing_L$ is the Thiele's modulus, which characterizes the reaction transport process for a given geometry. Thiele's modulus for chemical reactions can be found as:

$$\varnothing_L = \frac{r_{agg}}{3}\sqrt{\frac{k_c}{D_{eff,O_2}}} \qquad [16]$$

where D_{eff,O_2} is the effective diffusivity of dissolved reactant (O_2) in Nafion^{TM} presented in the agglomerate core and is approximated by using Bruggeman's relation.[53,54] The equation describing proton transport can be derived with the electro-neutrality assumption, which is then reduced to Ohm's law, i.e.,

$$\nabla \cdot (D_{\varnothing}^{eff} \nabla \cdot \varnothing_m) = \nabla \cdot i \qquad [17]$$

where $D_{\varnothing}^{eff}$ is the effective diffusion coefficient of proton conductivity, and $\varnothing_m$ is the electrolyte potential.

Macroscale model.—The macroscale model used in this work obtains the transport properties of the bipolar plate, the flow channel, and the proton exchange membrane (PEM) under unsteady-state conditions. The mass flow conditions and corresponding water activities in the porous medium will be obtained by the macroscale model combined with the calculation of electro-osmotic drag coefficient, net water flux per proton, and membrane conductivity. This model is a Navier–Stokes equation-based that incorporate mass, momentum, energy, and species transport equations. A commercial flow solver (Siemens/STAR-CD 2019.1.1) is used to perform the numerical analysis, to solve the coupled governing equations, and to share the transport properties as the boundary conditions to the HLBAM model.

Computational model.—In this work, 3D time dependent, HLBAM simulations of multi-physics/species transport and electrochemical kinetics inside porous and catalyst layers for PEMFCs with the multiphase flow model were run for these GDL, MPL, CL, and HCM. The Bhatnagar-GrossKrook (BGK) approximation with multiple-relaxation-time (MRT) collision operators of LBM is used to address the numerical stabilities of simulation in the micro and nano-scale detailed geometries.[55] The twenty-seven velocity (*D3Q27*) lattice model was used in this work. LBM is the particle-based model, the lattice size of GDL and MPL was set at 1.33 μm. The adaptive lattice spacing technique was applied to the surface of the CL and HCM with a lattice size of 10 nm. The surface tension of liquid was set to 0.072 N m^{-1}, which corresponds to the surface tension of water in contact with air at 20 °C. Surface tension is also liable for the contact angle where a surface meets a GDL surface. The fluid-fluid, fluid-air, and fluid-solid interface was determined by the interactions across these interfaces. The contact angle in the simulation was assumed to be constant and uniform distribution at 110°. This simulation is time dependent. The time step was set to 0.001 micro-second per time step for the HLBAM model and 1.00 millisecond per time step for the macroscale model. The multiphase flow model with particle-based tracking was selected to solve the interaction between two fluids at different scales with different transport properties. Large Eddy Simulation (LES) with local wall-adapting turbulent model was used in this simulation. The commercial software XFlow 2020 Refresh 1 Beta (Build 108.07) was used to perform the simulation on the LBM coupled with the macroscale model (Siemens/Star-CD). As mentioned earlier, the kinetics and mass transport information from the macroscale model was applied as a boundary condition at the interface boundary, as shown in Fig. 2. MATLAB® coupled with the transport data from LBM was used to perform the agglomerate simulation in the CL and HCM. Through this modeling method, the local transport behavior and characteristics of the reactant gases and products were investigated under various operating conditions. The porous medium model was applied to the MPL. The Darcy-Ergun equation[11] was employed to determine the pressure drop across the porous medium and simulate the mass transport inside the MPL.[56] The overall heat and mass transport in porous and catalyst layers are governed by the Boltzmann transport equation with the source term of the chemical reaction, which is an integral-differential equation of time, real space, and phase space. The electrochemical parameters used by this model are reported in Table I.

The cathode side of the PEMFC seems to have several problems that occur such as mass transport limitation, gas starvation, and partial flooding, which need to be explained. So, the cathode side of the cell was a primary focus and used to perform HLBAM simulation. Figure 3a shows an overview of the computational domain in this work. The top left figure shows the 50-cm^2 parallel flow-field with different study 3 locations (i.e., near inlet, middle, and near the exit). For operating conditions, the cell was operated with a current density of 1.0 A cm^{-2} and maintained the temperature at 60 °C with a relative humidity of 100%. The air-gas was fed to the cathode with the stoichiometric ratio of 15.0 at 1 bar. The dewpoint temperature of this operation was set at 60 °C with a system pressure of 251 kPa. A total of 6,400 catalyst sites on the CL were used as a

Table 1. Electrochemical reaction kinetics and agglomerate model parameters.

Parameter	Symbol	Value	Units	References
Agglomerate radius	r_{agg}	50[a)]	nm	
Effective Agglomerate surface area	a_{agg}	3,600[a)]	cm^2 cm^{-3}	51
CL Porosity	ε_{CL}	0.460	—	
GDL Porosity	ε_{GDL}	0.780	—	
CL Thickness	t_{CL}	9	μm	
Ionomer thin-film thickness	δ	8[a)]	nm	14
CL active surface area of Pt	a_{Pt}	4.382×10^4	cm^2 cm^{-3}	
Pt loading	m_{Pt}	0.300	mg cm^{-2}	
Thermal conductivity of GDL	k_{GDL}	0.12	W m.K^{-1}	57
Thermal conductivity of MPL	k_{MPL}	0.10	W m.K^{-1}	58
O_2 diffusion coef. in Nafion^{TM}	D_{O_2}	8.450×10^{-6}[a)]	cm^2 s^{-1}	46
H_2 diffusion coef. in Nafion^{TM}	D_{H_2}	2.000×10^{-6}[a)]	cm^2 s^{-1}	9
Henry's constant	H	3.166×10^{10}	Pa.cm^3 mol^{-1}	46
Reference O_2 concentration	$C_{O_2}^{ref}$	8.500×10^{-7}	mol cm^{-3}	46
Reference H_2 concentration	$C_{H_2}^{ref}$	5.640×10^{-5}	mol cm^{-3}	9
Cathode Ref. exchange current density	$i_{o,c}^{ref}$	1.500×10^{-6}	A cm^{-2}	46
Anode Ref. exchange current density	$i_{o,a}^{ref}$	2.295×10^{-3}	A cm^{-2}	14

a)—This is a reference value for the first loop of calculation. Then the model uses the local effective parameters to perform the calculation.

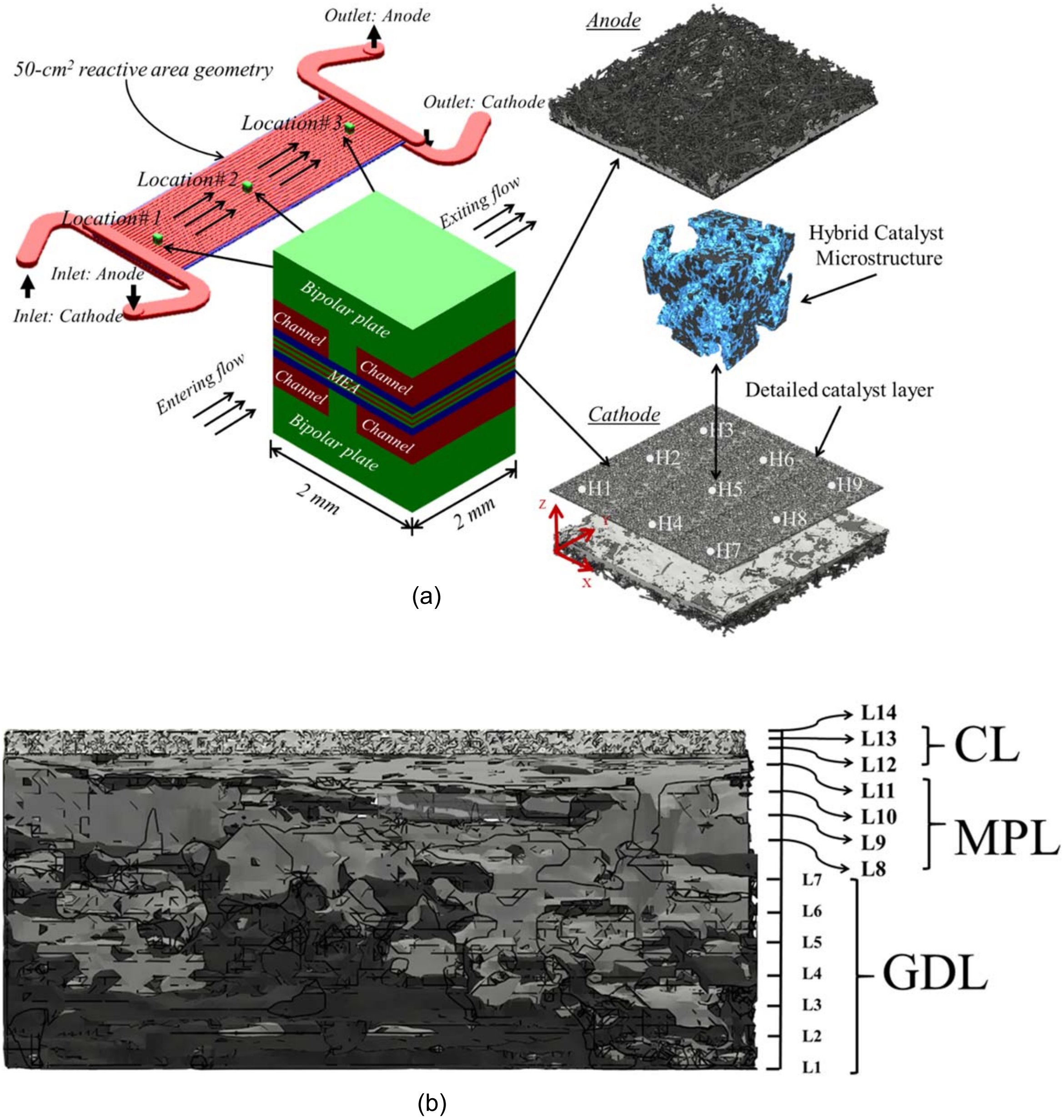

Figure 3. (a) Details of multiscale model of 50-cm^2 reactive area geometry. Macroscale model: 23 Straight channels flow-field with bipolar plates and MEA (3 different study locations), Microscale LBM: SGL 25BC, and Nanoscale HLBAM (9 different study locations): CL Ion Power with hybrid catalyst microstructure. (b) Cross section of GDL/MPL/CL sample showing fourteen layers used for the analysis of the distribution of transport variables.

reference site to perform the calculation along within the HCM. In this work, 9 sub-locations (i.e., H1 to H9) on the detailed structure CL were chosen to present as an illustration case of HLBAM simulation, as shown at the bottom right of Fig. 3a. Once again, these 9 sub-locations were selected from 6,400 catalyst sites that can represent the overall effect of geometry location on the mass transport such as land and channel. Sub-locations H1 to H3 and H7 to H9 represent the catalyst site across the channel area on the left and right of the detailed structure CL, respectively. Sub-locations H4 to H6 represents the catalyst site across the land area of the detailed structure CL. Figure 3b shows a cross-section of the porous sample, which is sliced into fourteen layers. Layers 1 to 7 represent the location of GDL, Layers 8 to 11 represent the location of MPL, and Layers 12 to 14 represent the location of CL. These layers are used as reference positions for analyzing the distribution of transport properties such as temperature, O_2 mass fraction, and liquid saturation. Note that, the maximum computational time was 18 h using 20 cores in a single node of an Intel Xeon 2.8 GHz with 256 GB RAM.

Results and Discussion

Figure 4 shows the polarization curve of a 50 cm^2 single cell under the same operating conditions mentioned above as a comparison between the three different simulation techniques and experiments. The result shows that all simulation techniques have similar predictions from the open-circuit voltage (OCV) to 0.1 A cm^{-2}. This is because the activation loss plays a major role in this cell operating range. All simulation techniques should provide similar results. There is no significance in the model prediction and comparison. For 0.1 to 0.6 A cm^{-2} of cell operating condition, HLBAM presents good agreement with the experimental data and shows better prediction than the other models. This might be the local transport properties that are included in the HLBAM calculation which shows

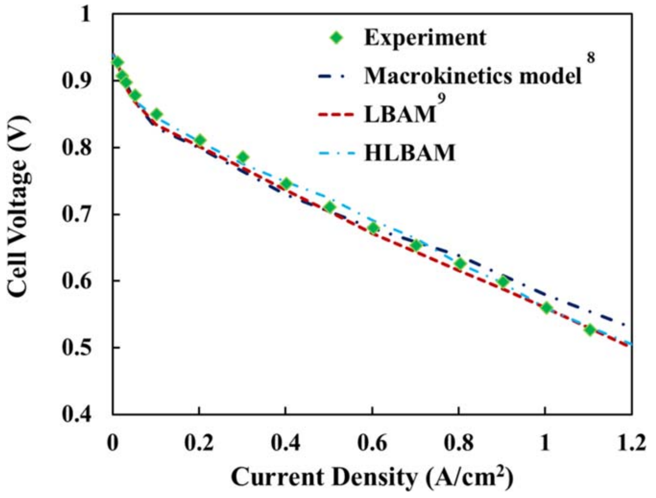

Figure 4. Polarization curves comparison between experimental result, macrokinetics model, LBAM, and HLBAM.

the significant impact on the potential losses in the CL. Since the model consists of the HCM, HLBAM included the local effective diffusivity of O_2 in the ionomer and air phase, which is provided a better prediction of electrochemical kinetic on the CL. Moreover, the simulation shows that the accuracy of the effective area of the CL can enhance the overpotential and current density distribution prediction. At high current density (i.e. current density starting from 0.6 A cm^{-2}), where the mass transport loss is dominant. HLBAM and LBAM show a similar prediction but HLBAM has a slightly better prediction than the other models. This is because the potential loss of both LBM models is higher than the macro-kinetics model due to the low partial pressure of O_2 gas, which provided high saturation pressure and a high amount of liquid water production. The macroscale model uses the entire prediction in the homogeneous GDL, MPL, and CL. No morphology affects the local transport prediction. Thus, HLBAM is a highly effective technique for determining the heat, mass, and electrochemical kinetics transport that affect the overall cell performance in the PEMFC.

Figure 5 shows the prediction of O_2 mass fraction distribution in the detailed structure of GDL, MPL, CL, and the HCM by using HLBAM simulation. The simulation results predict the behavior of O_2

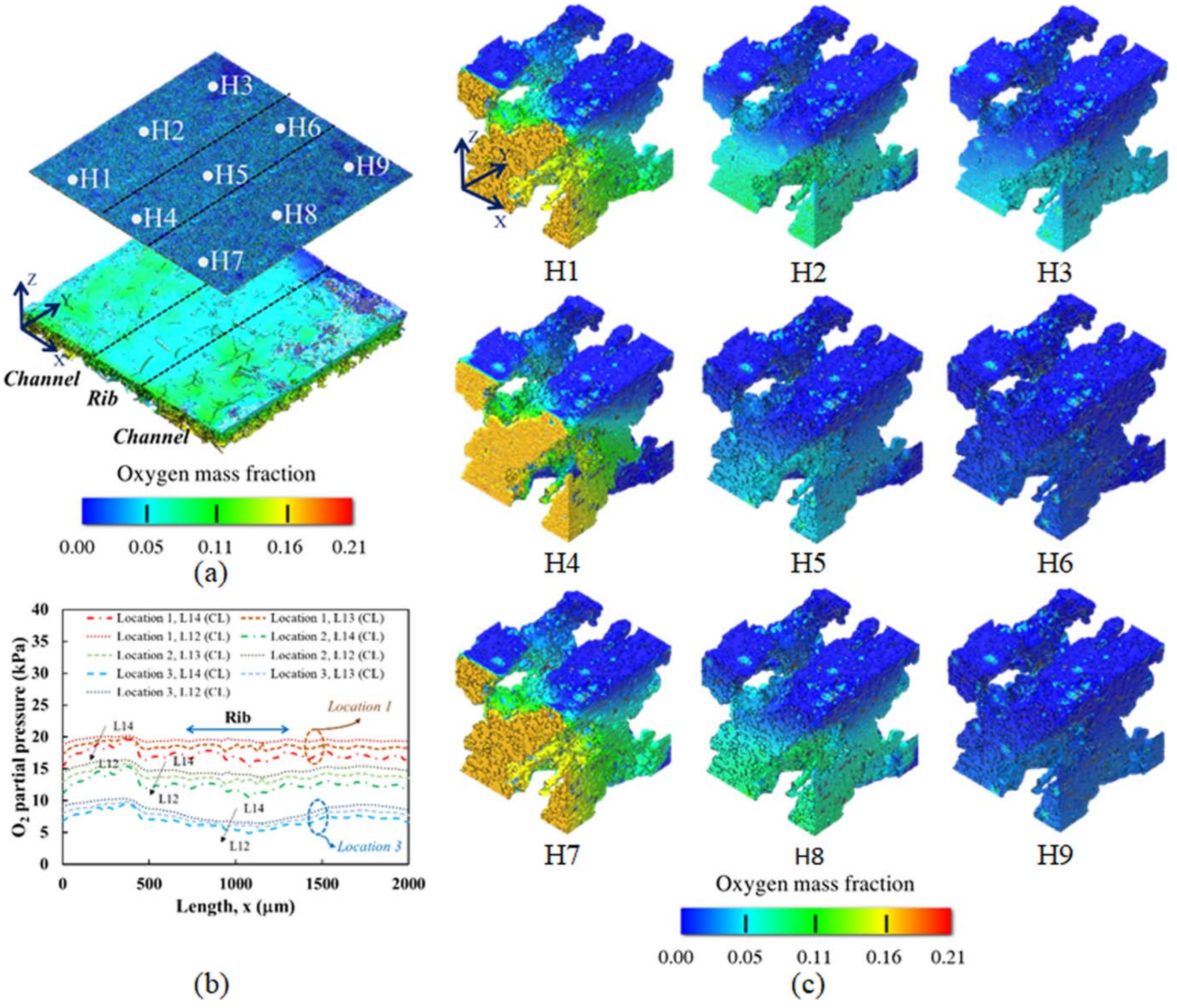

Figure 5. (a) Prediction of oxygen distribution within the detailed structure of GDL, MPL, CL at location 3, (b) Oxygen partial pressure profiles on the detailed structure for CL at 3 different locations, and (c) Predictions of oxygen mass fraction distribution within the hybrid catalyst at location 3.

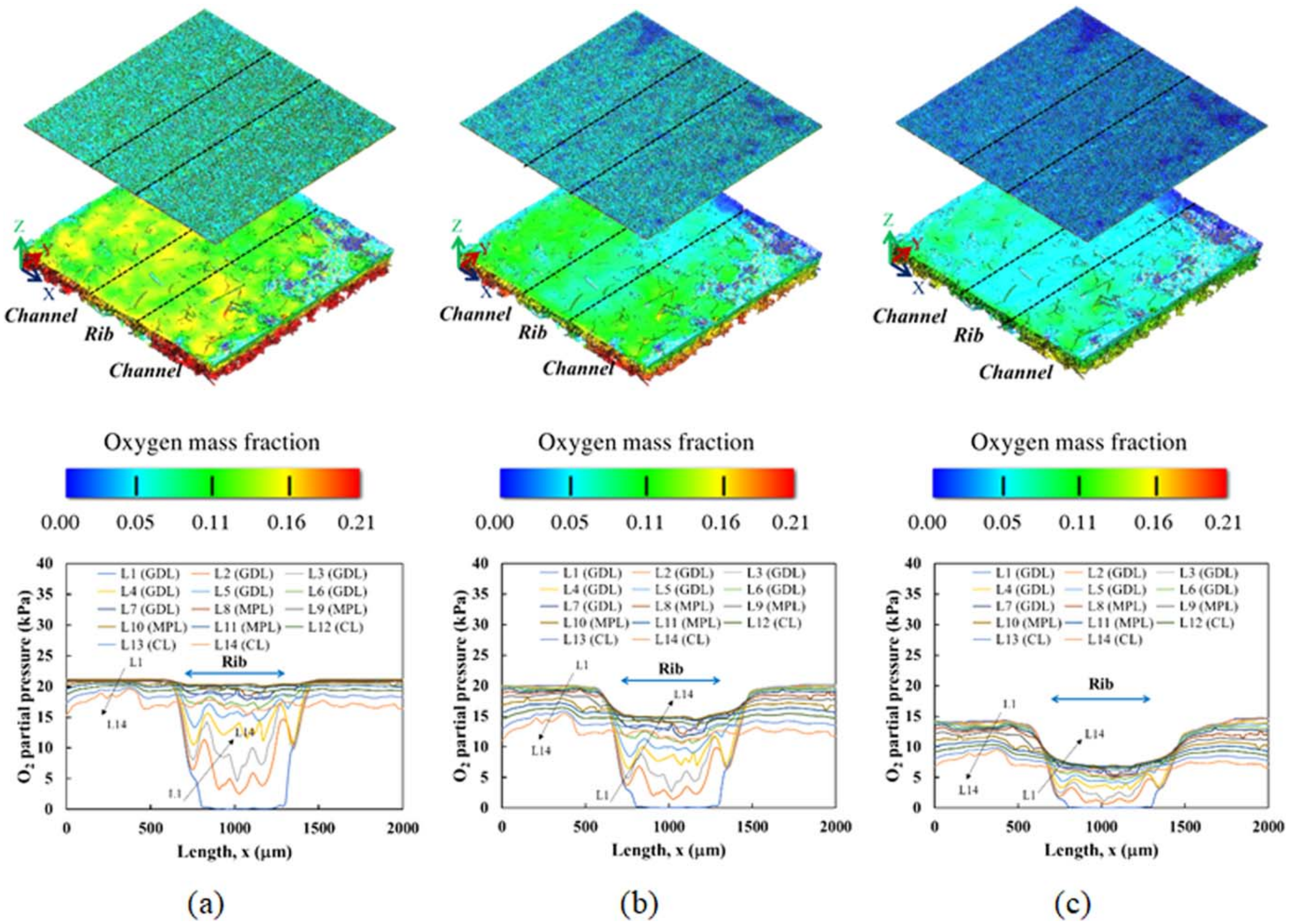

Figure 6. Predictions of oxygen mass fraction distribution and oxygen partial pressure profiles for three study locations under an average current density of 1 A cm^{-2}. (a) Location 1, (b) Location 2, and (c) Location 3.

transport at location 3 of the 50-cm^2 cell, where the exit region is located. Once again, location 3 was selected to examine the transport behavior because this location is expected to begin high mass transport loss. The current density was held at 1 A cm^{-2} with the potential of 0.675 V. The HLBAM simulation was parallelly calculated in both detailed structures of the CL and HCM. As mentioned above, the co-simulation approach with the data mapping method was used to simulated and bridged the data from 9 different sub-locations (i.e., H1 to H9) on the detailed structure CL. Figure 5a shows the O_2 distribution on the detailed structure of GDL, MPL, and CL. There is a higher O_2 mass fraction at the areas under the channel compared with the areas under the land (rib). Oxygen mass fraction decreases from channel/GDL interface toward CL, as its loss in transports into the GDL and MPL. After the O_2 reaches the CL, it is consumed and produced water by electrochemical reaction,[9] as a low O_2 mass fraction was observed in the CL. Figure 5b shows the prediction of O_2 partial pressure of 3 different locations within the CL. The overall prediction shows that there is lower O_2 partial pressure at the interface CL/MPL than the CL/PE-membrane interface. Location 1 shows the highest O_2 partial pressure and it decreases along within the gas transport pathways to the exit area at location 3. The low O_2 partial pressure at the exit area results from high vapor partial pressure. This is the effect of the pressure losses which is caused by the friction and momentum transfer resulting from a change in the direction and path of the flow along the flow-field. There should be a lot of liquid saturation in this location. The local O_2 distribution on HCM was depicted as shown in Fig. 5c. The results confirm that there is a low O_2 mass fraction under the rib area, as presented in sub-location H4 to H6. The HCM under both channel areas shows a similar local distribution of O_2 mass fraction, as shown in sub-locations H1 to H3 and H7 to H9. This might be due to the lower current density with lower oxygen partial pressure under the rib than under the channel area. The low oxygen mass fraction at the rib area is caused by the accumulation of liquid water saturation. Therefore, this area has lower oxygen partial pressure because of the formation of liquid water when compared with the prediction at the area under the channel. The result shows a significant gradient of oxygen concentration from the front toward the back of the sample (e.g., location 3), which could not be found in the previous work.[9] At the front area of location 3 (H1, H4, and H7), the results also show similar O_2 distribution, where a slightly lower O_2 mass fraction is seen under the rib. The middle area (H2, H5, and H8) shows a lower O_2 mass fraction than the front area but still higher than the back area (H3, H6, and H9). From the overall results, this HLBAM simulation able to predict in more detail such as the effect of rib and channel to the O_2 distribution on the CL, which helps the researchers to improve the fuel cell performance and stability.

Figure 6 shows the prediction of O_2 mass fraction distributions (Top) and O_2 partial pressure profiles (Bottom) on the detailed structure of the porous sample with three different study locations. Location 1 is located near the inlet of the cell. The result shows a high O_2 mass fraction with high O_2 partial pressure, as shown in Fig. 6a. This is because the inlet area has plenty of reactance gases and there is no mass transport limited. At the middle area of the cell where location 2 is located, the result shows a decrease in O_2 content due to the consumption of O_2 at the CL, as shown in Fig. 6b. The O_2 partial pressure shows slightly lower than location 1. At location 3 of the cell where the exit region is located. There is a low of O_2 mass fraction at the CL, as shown in Fig. 6c. This is because the mass

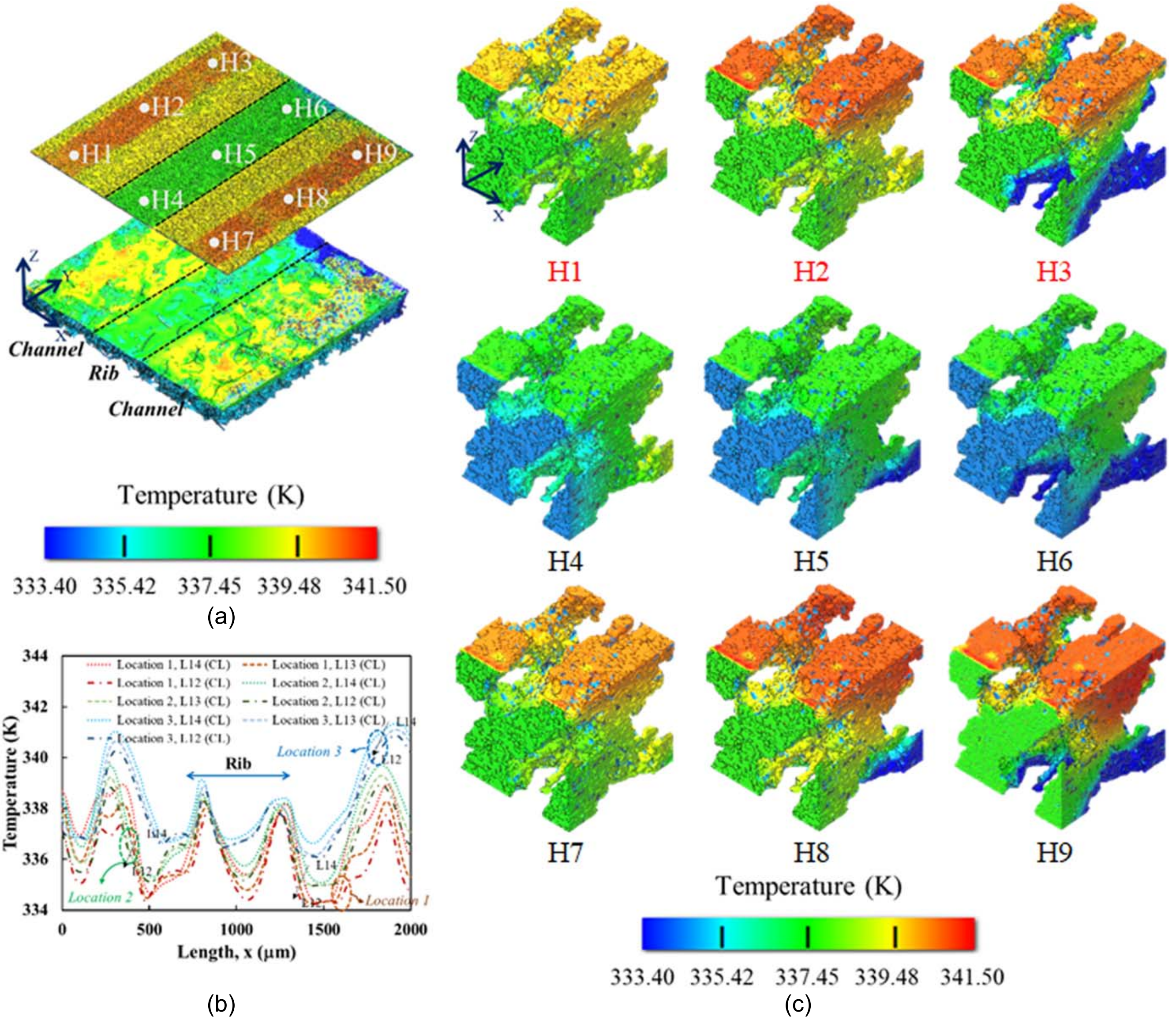

Figure 7. (a) Prediction of temperature distribution within the detail detailed structure of GDL, MPL, CL, (b) Oxygen partial pressure profiles on the detailed structure for CL different 3 study locations, and (c) Predictions of temperature distribution within the hybrid catalyst.

transport loss occurred at the downstream area. The O_2 mass fraction at the rib is lower than the channel area, which may be due to a high amount of condensed water and high-water vapor partial pressure in the rib area. In this operating condition, there is no influence from upstream consumption on the oxygen mass fraction due to high stoichiometric.[8] The condensed water will block the transport pores in the GDL/MPL, which not allowed the reactance gases to transport to the CL. The result also shows low O_2 partial pressure at the land area. This should be due to the high-water vapor partial pressure as the water is generated in the CL and liquid water condensation in the land area. These predictions were not found in the previous LBAM model.[9] After introducing the HCM, a better prediction of O_2 transport was revealed. For example, non-uniform of O_2 distribution on the detailed structure CL was observed, whereas the uniform O_2 distribution was observed in the previous LBAM model. The effect of non-uniform of O_2 distribution on the electrochemical kinetic expression will be discussed later in Fig. 13.

Figure 7 presents the heat transport in the detailed structure of porous samples of PEMFC and the HCM. Again, Location 3 was used to explore the local temperature distribution, as shown in Fig. 7a. At the CL, the observation indicates a high temperature at the channel area and a low temperature at the rib area. A similar temperature distribution was taken at the GDL/MPL. The low temperature under the rib area results from good heat transfer due to the higher thermal conductivity at the interface of GDL and rib. There is a high temperature at the interface of CL and PE membrane, where the electrochemical reaction mainly occurs. Heat is transferred from the CL to the bottom of GDL along with the temperature decrease throughout the entire thickness of the sample. This transport behavior is not similar to the previous model,[9] as more temperature gradient appears on CL. Thus, the local temperature distribution was investigated by using HCM with HLBAM. Figure 7b presents the temperature distribution on the CL. This figure also shows the temperature gradient at different layers along with the thickness of CL. This is because more chemical reactions were taking place in the CL/PE-membrane interface. Thermal properties can also be a factor in changing the temperature in these interfaces. The thermal conductivity of the catalyst layer is lower than the MPL about 0.03 W m-K^{-1},[59] which results in temperature at the CL/PE-membrane interface is higher than CL/MPL interface. Figure 7c shows the local temperature distribution on the HCM within different 9 sub-study locations on the detailed structure of

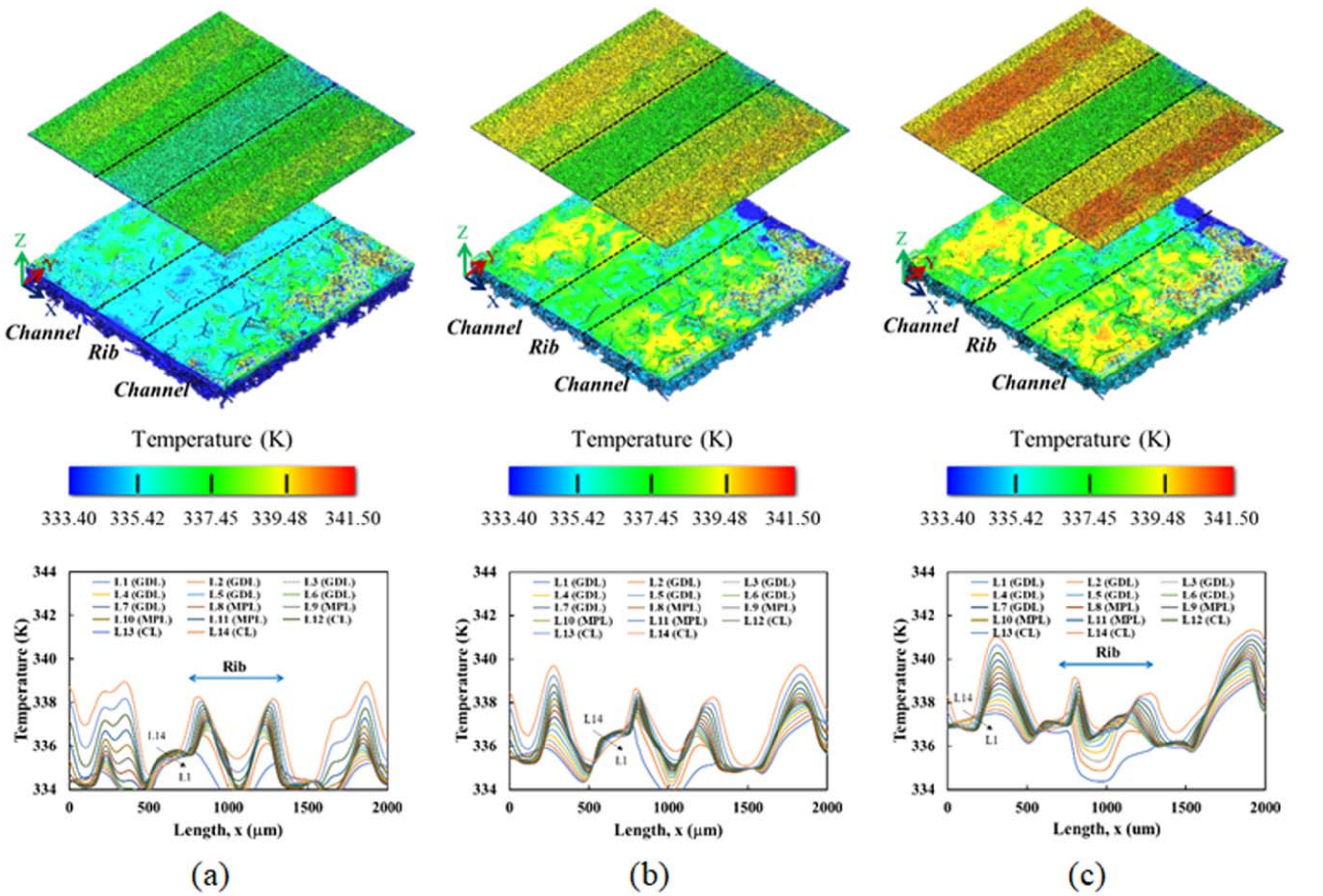

(a)

(b)

(c)

Figure 8. Predictions of temperature distribution and temperature profiles for three study locations under an average current density of 1 A cm^{-2}. (a) Location 1, (b) Location 2, and (c) Location 3.

CL. The results show a similar distribution as there is a high temperature at the channel area and low at the rib area. However, the temperature seems slightly high at the backside of the sample under the channel area (H1 to H3 and H7 to H9) though, it is not significant. Therefore, the maximum temperature is located at the sub-location H9 with the value of 340.27 K. There is a small temperature change under the rib area of the HCM (H4 to H6). Although there is no significant temperature change in the HCM, it also greatly involves the electrochemical kinetics prediction with the local transport properties.

Figure 8 summarizes the predictions of temperature distribution and temperature profiles for 3 different studied locations of 50 cm^2 cells. These figures on the top present the temperature distribution on the detailed structure CL whereas the figures on the bottom show the temperature profiles of each study location. The temperature profiles were determined by averaging the temperature from the in-plane (x-z planes) and along the through-plane (y-direction) for each thickness portion (i.e., 14 portions), as shown in Fig. 3b. Figure 8a shows the cathode temperature distribution prediction of location 1. This location has an average temperature on the GDL, MPL, and CL portions of 334.81, 335.24, and 336.26 K, respectively. Since this location lies near the inlet of the cell, the temperature is lower than the other locations. The surface temperature under the channel is also higher than the rib area, particularly at the CL, the same as location 3 mentioned above. This is because more reactance gases (O_2 in the cathode) are consumed exothermically under the channel. At the middle of the cell, which is presented by location 2, as shown in Fig. 8b. This location has a higher average temperature than Location 1. The average temperature of each portion from GDL to CL was reported with the value of 335.87, 336.24, and 336.83 K, respectively. Although the temperature is higher than a previous location, the distribution is similar. At the outlet area, where location 3 is located, as shown in Fig. 8c. This location has the average temperature of GDL, MPL, and CL about 337.08, 337.59, and 338.07 K, respectively. As already discussed above, this location has the highest temperature because it locates at the exit region where the mass transport loss occurs (i.e., the highest overpotential) due to the high accumulation of liquid water. Therefore, the highest heat generation caused by overvoltage or low local cell potential is appeared in this area.

The overall prediction of temperature distribution shows that there is a small change in temperature along with the thickness of the GDL/MPL and CL samples, which is approximately different 1 °C to 2 °C, as shown in the temperature profiles of Fig. 8. However, there is a significant change in temperature distribution at the CL when compared to the previous model.[9] In that model, the smooth temperature gradients and distribution were observed at the detailed CL, which results in the uniform distribution of electrochemical distribution. It seems like there is no effect of the morphology and the local transport properties on the kinetics modeling at CL using the LBAM model. After the HCM was introduced into the computational domain and become the HLBAM model, the prediction shows that there are more temperature gradient and distribution on the detailed structure of CL. The non-uniform temperature and O_2 distribution may result in an enhancement of physical electrochemical kinetic prediction in the detailed structure of CL.

Figure 9 shows the prediction of liquid water saturation on the detailed structure of locations 1 to 3. The volume of the liquid phase is used to represent the amount of liquid saturation inside the computational domain. The volume of liquid in the computational

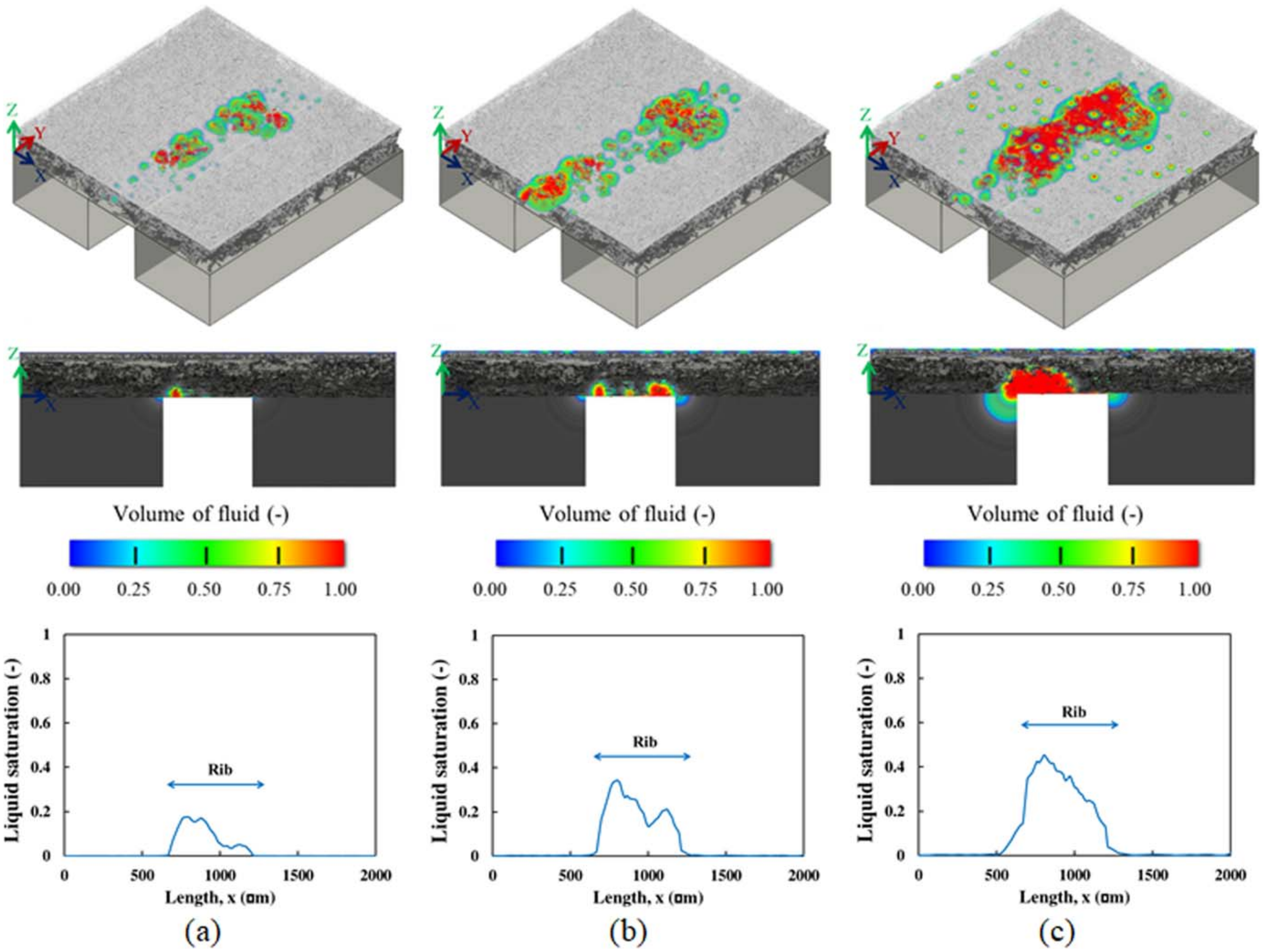

Figure 9. Predictions of liquid saturation and plot of liquid saturation profiles for three study locations under an average current density of 1 A cm^{-2}. (a) Location 1, (b) Location 2, and (c) Location 3.

domain has been calculated from the volume fraction of liquid water to the air (void phase) in the computational domain. The red color has a value of 1.00 which represents the 100% volume of liquid water, while the blue color represents 0%. The liquid water saturation in the porous layer is acquired by the chemical reaction and local condensation. When the partial pressure of water vapor is greater than the saturation pressure, the water vapor is saturated and condensed to be liquid water. From the overall results of this HLBAM simulation, most of the liquid saturation is occupied at the rib area. This is because the rib area has a lower temperature and a higher pressure than the channel area. At location 1, there is a low amount of liquid water accumulation under the rib area, as shown in Fig. 9a. The low amount of liquid saturation indicated that this area has low mass transport loss and still perform good local cell performance. Another reason that this area has less flooding occurs because this area is located near the inlet. In the general behavior of liquid water transport in the flow channel, when the liquid water is blown by the gas, the liquid water transports along the channel and accumulates toward the exit area. At the middle of the cell where location 2 is located, the result shows that the amount of liquid saturation is slightly higher than the inlet area, as shown in Fig. 9b. When considering liquid saturation with the temperature that has a small change along the thickness of the porous layers, there is also insignificant change of liquid water saturation along with the thickness of those layers. Hence, this can confirm that the temperature has a minor influence on the local liquid water saturation. Move to location 3 near the exit region, the result shows that this location has a lot of liquid water accumulation in the computational domain, as shown in Fig. 9c. Partial flooding might occur in this location. When comparing the distribution of liquid saturation with the previous model, these HLBAM simulation results are opposite. There is a high amount of liquid saturation occupied in the GDL area, not the MPL. There is a small amount of liquid saturation occurs at the MPL. This is because the MPL was treated with 5% −10% of the PTFE, which is a hydrophobic surface. Most of the water product from chemical reaction was blocked at the MPL/CL interface or transport pass through the crack of MPL. That is why not much liquid water present in the MPL region. The liquid saturation at the CL is from the chemical reaction that takes place in the CL region. The high saturation in the GDL is from the local condensation through high water vapor partial pressure. The results from the HLBAM model are consistent with the experimental data of Akitomo et al.,[57] that the liquid saturation presents more in the GDL underneath the rib area.

The overall transport prediction of O_2 partial pressure, O_2 mass fraction, temperature, and liquid saturation along with the thickness or the length of the sample are shown in Fig. 10. The profile of Figs. 10a, 10c, and 10d were calculated each single plane (x-z plane) for 1,000 planes along the y-direction. Average data of Fig. 10b was calculated from x-y plane along the z-direction. The O_2 partial pressure distribution along the length of the sample on the cathode side for locations 1 to 3 on 50 cm^2 cell are shown in Fig. 10a. The result shows that the O_2 partial pressure has low pressure under the rib area. This is because under the rib area has low temperature with

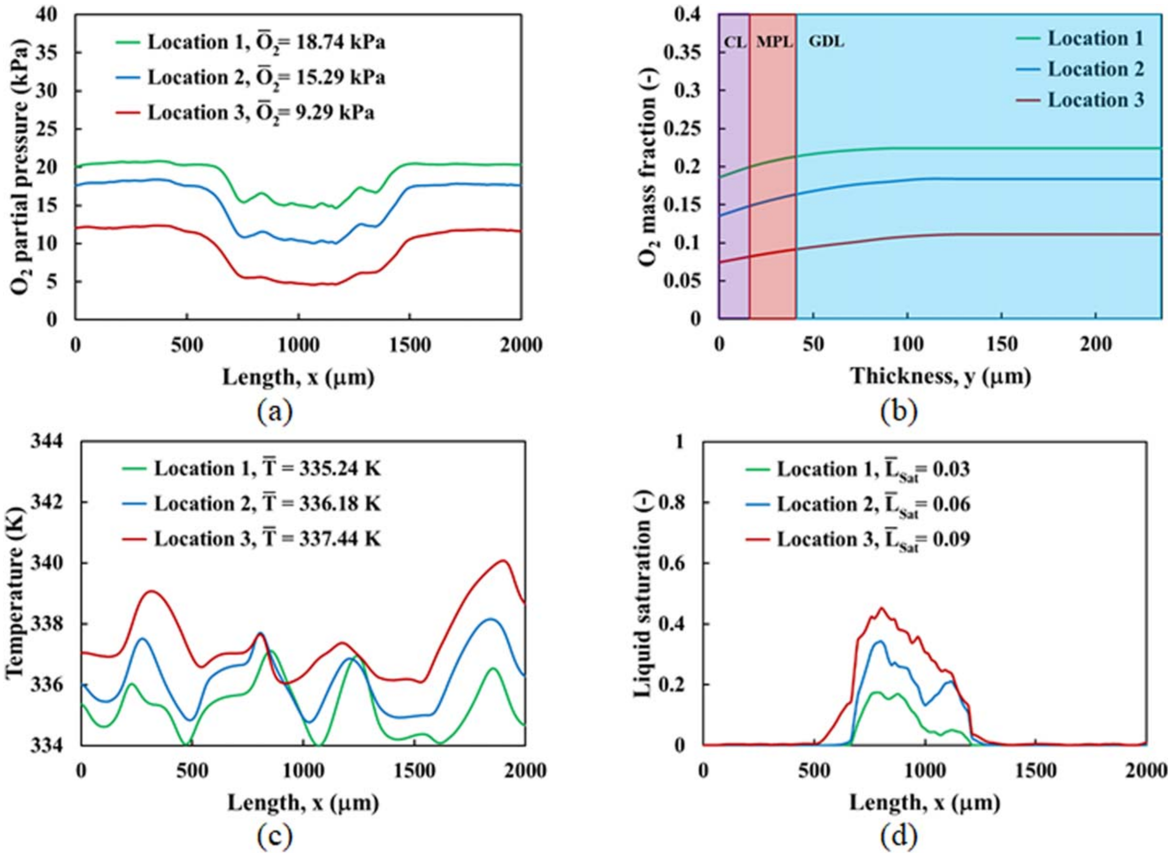

Figure 10. Overall transport prediction at 1 A cm^{-2}. (a) Oxygen partial pressure profiles across the length (x-direction) of the sample, (b) Oxygen mass fraction profiles across the thickness (z-direction) of the sample, (c) Cathode temperature profiles across the length (x-direction) of the sample, and (d) Cathode liquid saturation profiles across the length (x-direction) of the sample.

the high saturation pressure that led to water vapor saturation in this area. The overall distribution of O_2 partial pressure is the same. Location 1 has higher O_2 partial pressure than the other two locations because location 1 is located near the inlet, which has high pressure. Locations 2 and 3 have a descending in O_2 partial pressure respectively due to the mass transport loss and saturation of liquid water. Figure 10b presents the O_2 mass fraction across with the thickness of the sample for 3 different studied locations. When the O_2 enters the GDL from the channel, the O_2 transport in the GDL before moving into the MPL and then consumed in the CL. The simulation shows that the O_2 mass fraction drops crossing the interface from the GDL through the MPL. This shows the effect of the morphology change on the O_2 transport in the sample, where the reduced porosity in the MPL causes in step decrease at both interfaces of MPL. There is a high mass fraction near the inlet location, and it is reduced toward the middle and exit region. At the interface between the catalyst and PE membrane ($y = 0$ μm), locations 1 to 3 have O_2 mass fractions of 0.18, 0.14, and 0.07, respectively. The percent of O_2 consumption at these locations are 82%, 81%, and 68%, respectively. So, no flooding issue occurs in the cell with this operating condition.

For the overall temperature distribution of these 3 different locations, the average temperature profiles of the cathode are shown in Fig. 10c. The result shows that the temperature under the rib area is lower than the channel area. This is because the rib area has more conductive bipolar plate that allows better heat to transport toward the channel. The high temperature under the channel is due to the chemical reaction is favored under this area. This is because the reactance gases can easily flow through the GDL/MPL from the channel and react at the CL. The highest temperature is located near the exit region and the lowest temperature is found near the inlet region, caused by the heat generation along with the channel length. The liquid condensation seems to correlate with the temperature profiles, while the low temperature has low liquid saturation, as shown in Figs. 10c and 10d. Since the operating condition of simulation sets the temperature of 60 °C, the major impact on the amount of liquid saturation of this simulation is the distance of the transport channel or the study location. The downstream region, location 3 has more liquid water presented due to the water accumulation along the transport channel. The average liquid saturation at the locations 1 to 3 are 0.03, 0.06, and 0,09, respectively. The liquid saturation also correlates with the operating condition, as at high current density more water is produced. This is because high current density has a high ORR, which increases the water production rate. The overall prediction presents that the most liquid accumulation occurs around the middle of the GDL where the rib is located. This is because of the low temperature in this area and high-water saturation pressure that makes the water vapor easily condenses.

Figure 11 shows the simulation of O_2 effective diffusivity of the air and Nafion phase in the HCM. The simulation on HCM enables one to investigate the local transport properties such as effective diffusivity. The bridging technique is also used to transfer the data from the HCM to the detailed structure CL, which is enable the simulation to use the local transport properties to predict the electrochemical kinetic distribution. In the porous medium simulation, the diffusion coefficient in porous media is smaller than the bulk diffusion coefficient. Therefore, an effective diffusion coefficient was defined, which is based on the average cross-sectional open area to diffusion and the distance traveled by species molecule in the porous structure. The prediction shows that the average of O_2 effective diffusivity in the air (Pore) and Nafion (Solid) phase are 2.6×10^{-2} and 1.75×10^{-6} cm^2 s^{-1}, respectively. The result shows that the O_2 effective diffusivity in the Nafion phase at the sub-locations

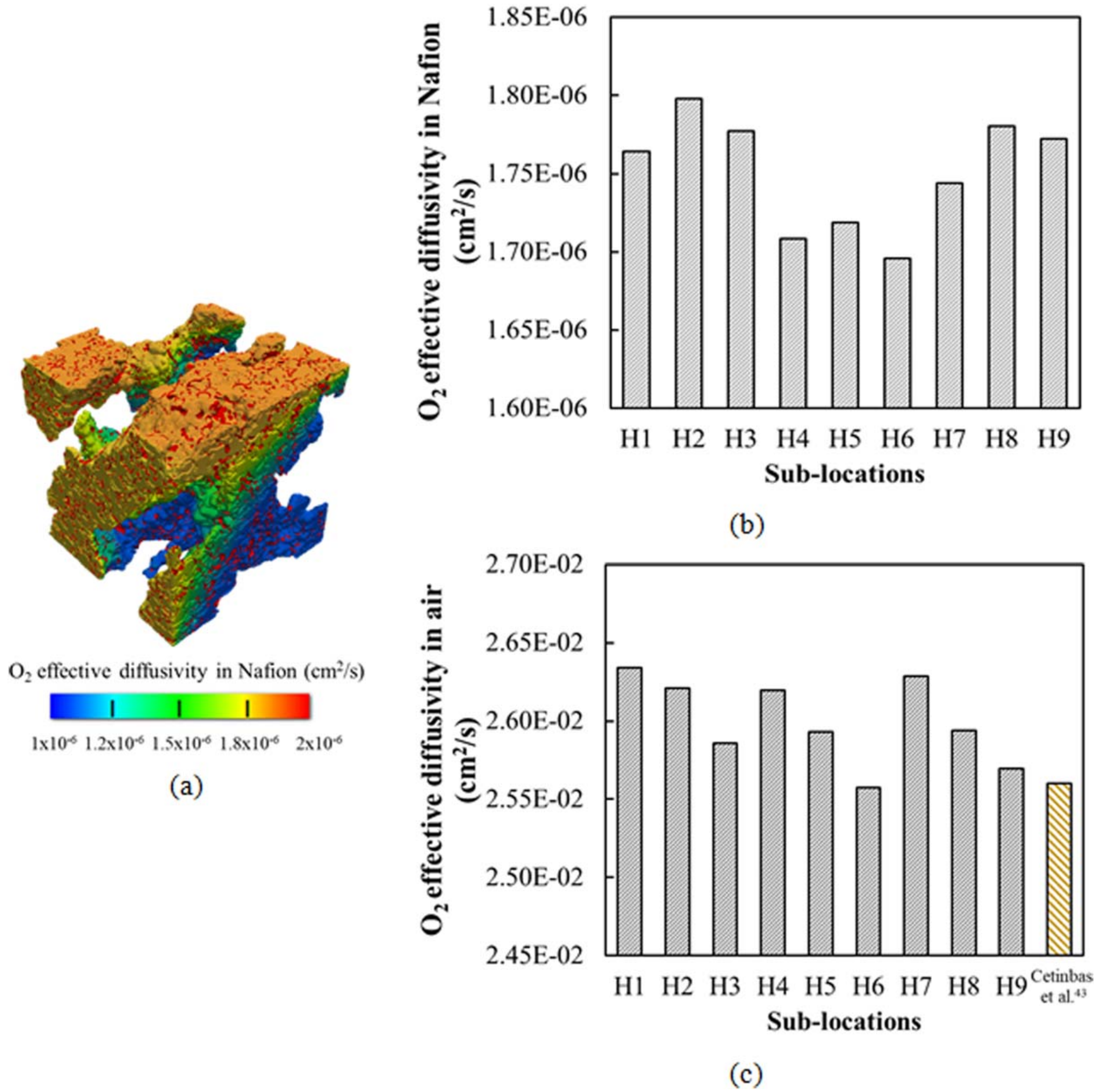

Figure 11. (a) Prediction of oxygen effective diffusivity in hybrid catalyst at sub-location H1 of location 3, (b) comparison of oxygen effective diffusivity in Nafion for 9 sub-locations, and (c) comparison of oxygen effective diffusivity in air for 9 sub-locations.

H4 to H6 has lower than the other location under the channel, as shown in Fig. 11b. This is because of the low temperature under the rib area, which is results in the low effective diffusivity in the Nafion phase. The effective diffusivity in the Nafion phase has been calculated by using Eq. 12 from Cetinbas et al.[43] This clearly shows that the temperature has a significant impact on the effective diffusivity in the liquid phase. For O_2 effective diffusivity in the air, the prediction shows that the location near the inlet has higher effective diffusivity than near the outlet area, as shown in Fig. 11c. This might be the effect of mass transport loss that occurs at the outlet area, which results in low diffusivity. When comparing this model prediction with Cetinbas's model[43] by using the same HCM geometry. The result shows that the average effective diffusivity of HLBAM is slightly higher than Cetinbas's model.[43] After introducing an HCM into HLBAM and applying the bridging technique to perform the simulation, the model exhibits an increase in the capability of the prediction in local transport behavior, which can provide more accuracy of overall prediction.

Figure 12 shows the prediction of electrochemical variables distribution in the different detailed components of the catalyst agglomerate such as ionomer, carbon, and platinum. Figures 12a and 12b show the prediction of cathode overpotential and current density distribution on the HCM, respectively. The sub-location H1 of location 3 is used to examine the surface plot of overpotential and current density. The prediction shows that there is a slightly uniform distribution of overpotential and current density on the detailed geometry surface. The current density is high in the area that has low overpotential, which follows Ohm's law. The low cell voltage can be occurred by the high overpotential required for the ORR.

If the surface of the CL shows high overpotential, the cell voltage will be dropped, and the current density will be decreased also. The average overpotential and current density are reported in Figs. 12c and 12d, respectively. There is a slight change of overpotential distribution throughout 9 positions with an average of 0.265 V. Interestingly that the current density has more non-uniform distribution, especially under the rib and channel area. Sub-locations H1-H3 and H7-H9 represent the site of the HCM under the channel area. Sub-locations H4-H6 stand for the site of HCM under the rib area. After the HCM is introduced into LBM, more parameters that affect the cell performance and transport behavior were explored. The result shows that there is a low current density under the rib area. This is because of a low amount of reactance gases (i.e., O_2) and flooding issue that might be occurred under the rib area, as shown in

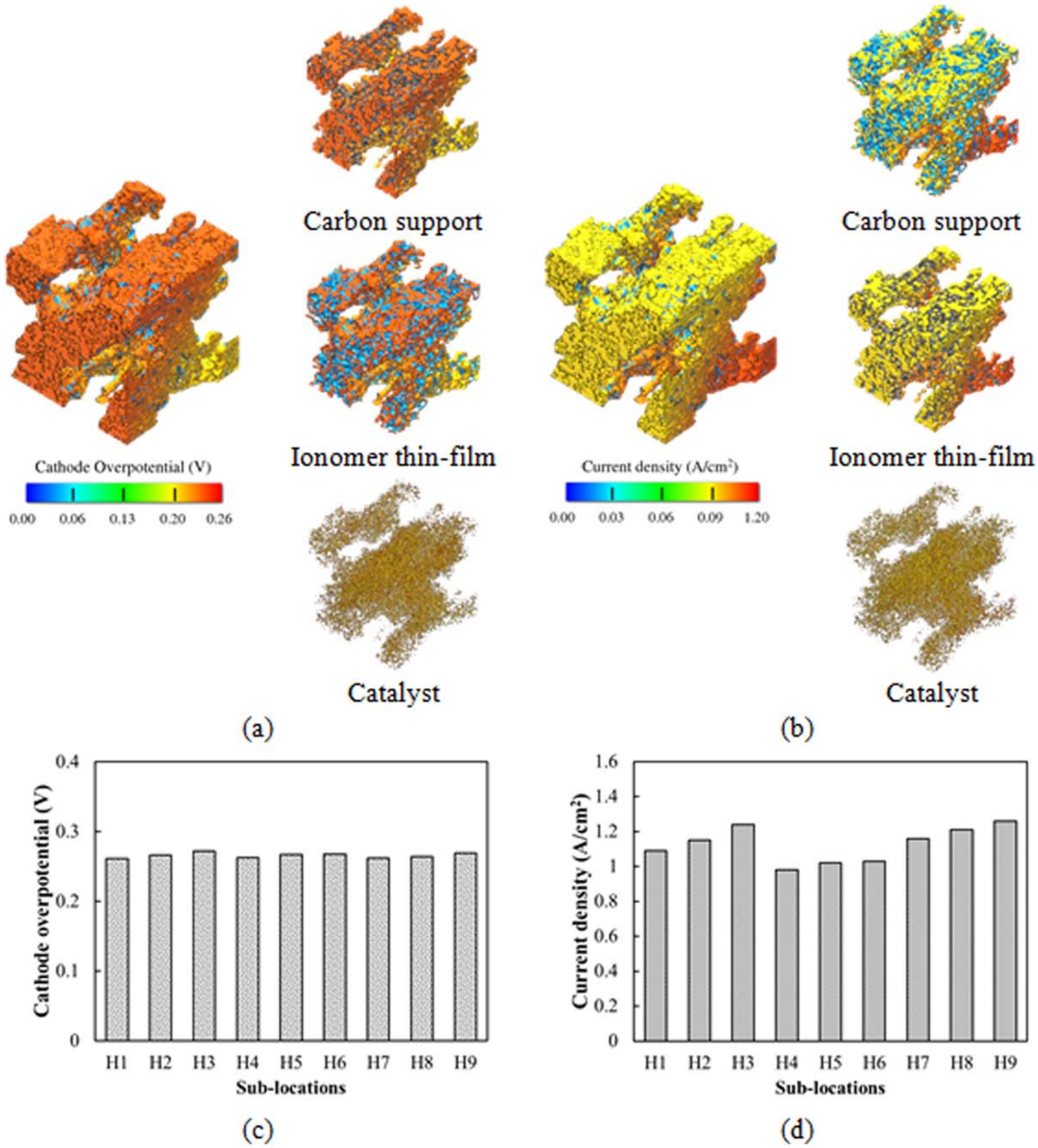

Figure 12. Prediction of cathode overpotential and current density distribution within the hybrid catalyst microstructure. (a) Cathode overpotential distribution at sub-location H1 of location 3, (b) current density at sub-location H1 of location 3, (c) Overall prediction of cathode overpotential.

Figs. 6 and 9. The O_2 transport pathways in the GDL are blocked by the liquid saturation under the rib area, which results in less gas transport to the CL. This transport behavior cannot capture by the previous model.[9]

Figure 13 shows the overall prediction of electrochemical kinetics distribution on the detailed structure of CL. The overpotential distributions of locations 1 to 3 were depicted and shown in Figs. 13a to 13c, respectively. There is a uniform distribution on the surface of the CL for all locations, which has a small effect on the land and channel. The result is consistent with the HCM that has uniform distribution for all sub-locations (H1 to H9) on the CL, as shown in Fig. 12c. The overpotential is steadily increasing from location 1 toward location 3, respectively. At location 3 where the exit region is located, the result shows the highest overpotential, which results in low potential under this area. This may be because of flooding issues and mass transport loss present near the exit region. As mentioned previously, the low O_2 effective diffusivity is another reason for mass transport loss that results in low cell performance. This can show the correlation of HCM on the detailed structure of the CL by using the bridging method. Locations 1 to 3 have the local potential of 0.59, 0.56, and 0.52, respectively. The cell potential drops from the inlet to the exit region, which is due to the mass transport loss in the cell. At the exit region where location 3 is located, the liquid saturation in the GDL substrate might block the transport pathways of the reactance gas. Therefore, location 3 has a high overpotential with low local potential. The plots of current density distribution on the detailed CL of locations 1 to 3 are shown in Figs. 13d to 13f, respectively. The model prediction shows that locations 1 to 3 have the average current density of 0.903, 0.983, and 1.128 A cm^{-2}, respectively. The overall prediction also shows that

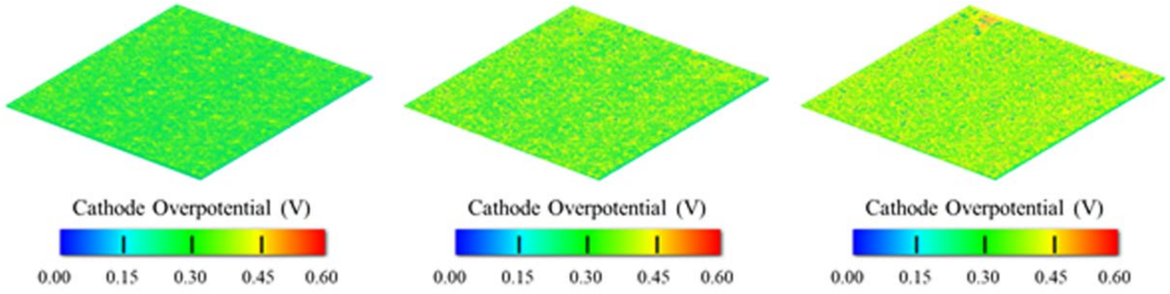

(a) $\eta_{c,\,ave} = 0.225$ V (b) $\eta_{c,\,ave} = 0.241$ V (c) $\eta_{c,\,ave} = 0.265$ V

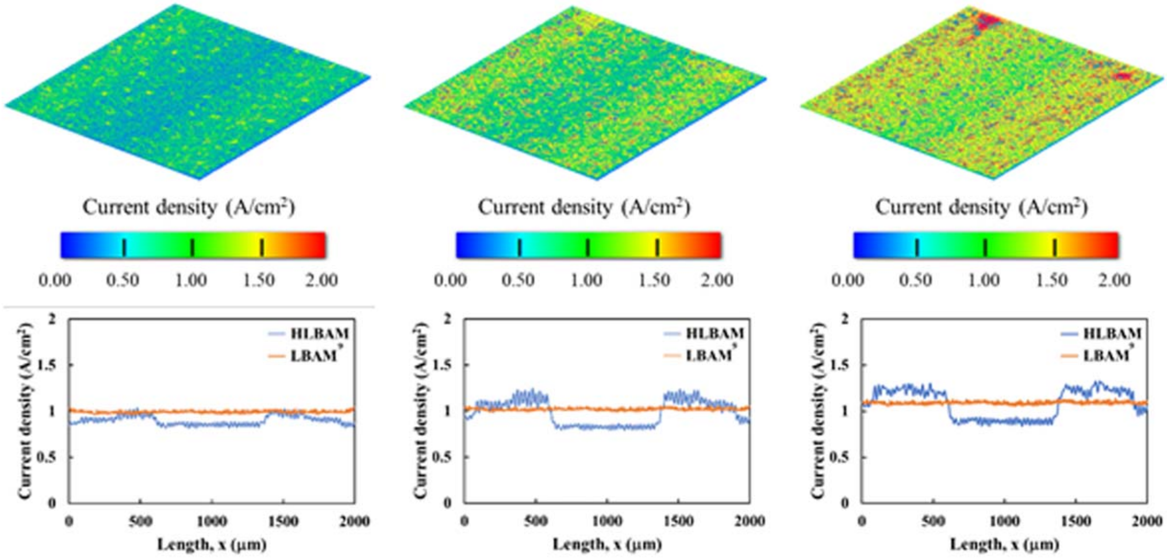

(d) $i_{ave} = 0.903$ A/cm² (e) $i_{ave} = 0.983$ A/cm² (f) $i_{ave} = 1.128$ A/cm²

Figure 13. Predictions of electrochemical distribution within the detailed structure of CL at locations 1 to 3. Cathode overpotential of (a) location 1, (b) location 2, and (c) location 3. Current density distribution and plot of current density along with the length of the sample for (d) location 1, (e) location 2, and (f) location 3.

there is a higher current density at the channel than the rib area. This is because more reactive gas can reach the CL. Another reason is that the liquid saturation more present under the rib area. This is the sign of mass transport loss and flooding issues, which result in low current density under the rib area. The modeling result from HLBAM shows more gradient of current distribution than the LBAM model.[9] More details of electrochemical kinetics prediction of PEMFC can be captured when the HCM is introduced into the LBM model.

Conclusions

Multi-scale modeling HLBAM is the direct modeling-based that has been demonstrated to explore the electrochemical kinetics and multi-scalar/physics transport inside the detailed structure of porous and catalyst layers of PEMFCs. This work shows the successful development of a new catalyst modeling technique that incorporates the detailed structure of CL and HCM. The unique aspect of this work is to integrate the lattice elements into an agglomerate structure in the nano-scale geometry of the CL. This work presents the enhancing the potential capability of the kinetics model by introducing the HCM into the electrochemical kinetics model, which be able to predict the local transport inside the CL. HLBAM enables to distinguish electrochemical distribution in the three-phase boundaries at the catalyst site. The bridging method has been developed to incorporate the local transport information between the HCM and local effective catalyst sites in the CL. The catalyst model with HLBAM shows a better match with experimental data, particularly it can capture mass transport overpotential accurately. Moreover, the HLBAM shows the ability to model other electrochemical systems as well, especially those with complex micro- or nano- structures such as other fuel cells, batteries, or electrolyzers.

Acknowledgments

This project was supported by the University Research Program of Ford Motor Company. The authors would like to acknowledge Dassault Systèmes Simulia S.L.U. for providing the XFlow software and Siemens Product Lifecycle Management Software Inc. for providing Star-CD software. This research used resources of the Advanced Photon Source (APS) to obtain the hybrid catalyst microstructure, a U.S. Department of Energy Office of Science User Facility operated for the DOE Office of Science by Argonne National Laboratory under Contract No. DE-AC02-06CH11357.

ORCID

P. Satjaritanun https://orcid.org/0000-0001-6458-2845
F. C. Cetinbas https://orcid.org/0000-0001-8592-4816
I. V. Zenyuk https://orcid.org/0000-0002-1612-0475
R. K. Ahluwalia https://orcid.org/0000-0002-9031-1907
S. Shimpalee https://orcid.org/0000-0002-7418-9526

References

1. Y. Wang, D. F. Ruiz Diaz, K. S. Chen, Z. Wang, and X. C. Adroher, *Mater. Today*, **32**, 178 (2020).
2. E. Ogungbemi, T. Wilberforce, O. Ijaodola, J. Thompson, and A. G. Olabi, *Int. J. Hydrogen Energy* (2020).

3. F. Zhao, Z. Mu, H. Hao, Z. Liu, X. He, S. V. Przesmitzki, and A. A. Ameret, *Energy Technol.*, **8**, 2000179 (2020).
4. M. Muthukumar, N. Rengarajan, B. Velliyangiri, M. A. Omprakas, C. B. Rohit, and U. K. Raja, *Mater. Today Proc.* (2020).
5. J. M. Ogden, M. M. Steinbugler, and T. G. Kreutz, *J. Power Sources*, **79**, 143 (1999).
6. S. Dutta, S. Shimpalee, and J. W. V. Zee, *Int. J. Heat Mass Transf.*, **44**, 2029 (2001).
7. K. Forrest, M. Mac Kinnon, B. Tarroja, and S. Samuelsen, *Appl. Energy*, **276**, 115439 (2020).
8. S. Shimpalee, P. Satjaritanun, S. Hirano, N. Tippayawong, and J. W. Weidner, *J. Electrochem. Soc.*, **166**, F534 (2019).
9. P. Satjaritanun, S. Hirano, I. V. Zenyuk, J. W. Weidner, N. Tippayawong, and S. Shimpalee, *J. Electrochem. Soc.*, **167**, 013516 (2020).
10. A. Z. Weber et al., *J. Electrochem. Soc.*, **161**, F1254 (2014).
11. P. Satjaritanun, J. W. Weidner, S. Hirano, Z. Lu, Y. Khunatorn, S. Ogawa, S. E. Litster, A. D. Shum, I. V. Zenyuk, and S. Shimpalee, *J. Electrochem. Soc.*, **164**, E3359 (2017).
12. P. Satjaritanun, S. Hirano, A. D. Shum, I. V. Zenyuk, A. Z. Weber, J. W. Weidner, and S. Shimpalee, *J. Electrochem. Soc.*, **165**, F1115 (2018).
13. S. Shimpalee and J. W. V. Zee, *Int. J. Hydrogen Energy*, **32**, 842 (2007).
14. S. Shimpalee, M. Ohashi, J. W. Van Zee, C. Ziegler, C. Stoeckmann, C. Sadeler, and C. Hebling, *Electrochim. Acta*, **54**, 2899 (2009).
15. S. Shimpalee and S. Dutta, *Numer. Heat Transf.*, **38**, 111 (2000).
16. S. Shimpalee, S. Hirano, M. DeBolt, V. Lilavivat, J. W. Weidner, and Y. Khunatorn, *J. Electrochem. Soc.*, **164**, E3073 (2017).
17. S. Shimpalee, V. Lilavivat, H. McCrabb, Y. Khunatorn, H.-K. Lee, W.-K. Lee, and J. W. Weidner, *Int. J. Hydrogen Energy*, **41**, 13688 (2016).
18. J. Liu, P. A. García-Salaberri, and I. V. Zenyuk, *Transp. Porous Media*, **128**, 363 (2019).
19. L. M. Pant and A. Z. Weber, *J. Electrochem. Soc.*, **164**, E3102 (2017).
20. A. Z. Weber and J. Newman, *J. Electrochem. Soc.*, **151**, A311 (2004).
21. W. Yoon and A. Z. Weber, *J. Electrochem. Soc.*, **158**, B1007 (2011).
22. I. V. Zenyuk, P. K. Das, and A. Z. Weber, *J. Electrochem. Soc.*, **163**, F691 (2016).
23. L. M. Pant, S. K. Mitra, and M. Secanell, *Int. J. Heat Mass Transf.*, **58**, 70 (2013).
24. A. Z. Weber and J. Newman, *Chem. Rev.*, **104**, 4679 (2004).
25. V. M. Ehlinger, A. R. Crothers, A. Kusoglu, and A. Z. Weber, *J. Phys.: Energy*, **2**, 044006 (2020).
26. A. Goshtasbi, P. García-Salaberri, J. Chen, K. Talukdar, D. G. Sanchez, and T. Ersal, *J. Electrochem. Soc.*, **166**, F3154 (2019).
27. J. Gostick et al., *Comput. Sci. Eng.*, **18**, 60 (2016).
28. Z. A. Khan, P. A. Garcia-Salaberri, T. M. M. Heenan, R. Jervis, P. R. Shearing, D. Brett, A. Elkamel, and J. T. Gostick, *J. Electrochem. Soc.*, **167**, 040528 (2020).
29. T. Agaesse, A. Lamibrac, F. N. Büchi, J. Pauchet, and M. Prat, *J. Power Sources*, **331**, 462 (2016).
30. T. G. Tranter, P. Boillat, A. Mularczyk, V. Manzi-Orezzoli, P. R. Shearing, D. J. L. Brett, J. Eller, J. T. Gostick, and A. Forner-Cuenca, *J. Electrochem. Soc.*, **167**, 114512 (2020).
31. I. V. Zenyuk, E. Medici, J. Allen, and A. Z. Weber, *Int. J. Hydrogen Energy*, **40**, 16831 (2015).
32. E. F. Medici, I. V. Zenyuk, D. Y. Parkinson, A. Z. Weber, and J. S. Allen, *Fuel Cells*, **16**, 725 (2016).
33. F. C. Cetinbas, R. K. Ahluwalia, A. D. Shum, and I. V. Zenyuk, *J. Electrochem. Soc.*, **166**, F3001 (2019).
34. M. Sepe, P. Satjaritanun, S. Hirano, I. V. Zenyuk, N. Tippayawong, and S. Shimpalee, *J. Electrochem. Soc.*, **167**, 104516 (2020).
35. E. Shakerinejad, M. H. Kayhani, M. Nazari, and A. Tamayol, *Int. J. Hydrogen Energy*, **43**, 2410 (2018).
36. D. H. Jeon, *J. Energy Inst.*, **92**, 755 (2019).
37. D. H. Jeon and H. Kim, *J. Power Sources*, **294**, 393 (2015).
38. P. A. García-Salaberri, J. T. Gostick, G. Hwang, A. Z. Weber, and M. Vera, *J. Power Sources*, **296**, 440 (2015).
39. P. A. García-Salaberri, I. V. Zenyuk, A. D. Shum, G. Hwang, M. Vera, A. Z. Weber, and J. T. Gostick, *Int. J. Heat Mass Transf.*, **127**, 687 (2018).
40. W. K. S. Chiu, A. S. Joshi, and K. N. Grew, *Eur. Phys. J. Spec. Top.*, **171**, 159 (2009).
41. B. Han, M. Ni, and H. Meng, *Entropy*, **18**, 1 (2016).
42. D. Zhang, Q. Cai, and S. Gu, *Electrochim. Acta*, **262**, 282 (2018).
43. F. C. Cetinbas, R. K. Ahluwalia, N. Kariuki, V. De Andrade, D. Fongalland, L. Smith, J. Sharman, P. Ferreira, S. Rasouli, and D. J. Myers, *J. Power Sources*, **344**, 62 (2017).
44. F. C. Cetinbas and R. K. Ahluwalia, *J. Electrochem. Soc.*, **165**, F1059 (2018).
45. F. C. Cetinbas, R. K. Ahluwalia, N. N. Kariuki, and D. J. Myers, *J. Electrochem. Soc.*, **165**, F1051 (2018).
46. A. El-Kharouf, T. J. Mason, D. J. L. Brett, and B. G. Pollet, *J. Power Sources*, **218**, 393 (2012).
47. W. Sun, B. A. Peppley, and K. Karan, *Electrochim. Acta*, **50**, 3359 (2005).
48. J. Zhou, S. Shukla, A. Putz, and M. Secanell, *Electrochim. Acta*, **268**, 366 (2018).
49. M. Moore, A. Putz, and M. Secanell, *J. Electrochem. Soc.*, **160**, F670 (2013).
50. R. Pavlicek, S. C. Barton, N. Leonard, H. Romero, S. McKinney, G. McCool, A. Serov, D. Abbott, P. Atanassov, and S. Mukerjee, *J. Electrochem. Soc.*, **165**, F589 (2018).
51. F. C. Cetinbas, S. G. Advani, and A. K. Prasad, *J. Electrochem. Soc.*, **160**, F750 (2013).
52. F. C. Cetinbas, S. G. Advani, and A. K. Prasad, *J. Power Sources*, **250**, 110 (2014).
53. D. Harvey, J. G. Pharoah, and K. Karan, *J. Power Sources*, **179**, 209 (2008).
54. M. Moore, P. Wardlaw, P. Dobson, J. J. Boisvert, A. Putz, R. J. Spiteri, and M. Secanell, *J. Electrochem. Soc.*, **161**, E3125 (2014).
55. D. M. Holman, R. M. Brionnaud, and Z. Abiza, *ECCOMAS proceeding* (2012).
56. S. Chen and G. Doolen, *Annu. Rev. Fluid Mech.*, **30**, 329 (1998).
57. F. Akitomo, T. Sasabe, T. Yoshida, H. Naito, K. Kawamura, and S. Hirai, *J. Power Sources*, **431**, 205 (2019).
58. A. Thomas, G. Maranzana, S. Didierjean, J. Dillet, and O. Lottin, *Int. J. Hydrogen Energy*, **39**, 2649 (2014).
59. O. S. Burheim, H. Su, H. H. Hauge, S. Pasupathi, and B. G. Pollet, *Int. J. Hydrogen Energy*, **39**, 9397 (2014).